Synthesis of artificial cells *via* biocatalytic polymerisation-induced self-assembly

Sètuhn Jimaja,[a‡] Andrea Belluati,[b,c‡*] Robert J. Chadwick,[b] Christopher Glynn,[b] Mohamed Chami[d], Dominic Happel[c], Chao Guo[b], Harald Kolmar[c], and Nico Bruns[b,c*]

[a]Adolphe Merkle Institute, University of Fribourg, Chemin des Verdiers 4, 1700 Fribourg, Switzerland.
[b]Department of Pure and Applied Chemistry, University of Strathclyde, Thomas Graham Building, 295 Cathedral Street, Glasgow G1 1XL, United Kingdom.
[c]Department of Chemistry and Centre for Synthetic Biology, Technical University of Darmstadt, Peter-Grünberg-Straße 4, 64287 Darmstadt, Germany.
[d]Biozentrum, University of Basel, Spitalstrasse 41, 4056 Basel, Switzerland.

‡Authors contributed equally to this work

*andrea.belluati@tu-darmstadt.de, nico.bruns@tu-darmstadt.de

ABSTRACT

Artificial cells are biomimetic microstructures that mimic functions of natural cells and find application, e.g., as microreactors, as building blocks for molecular systems engineering, and to host synthetic biology pathways. Here, we report enzymatically synthesised polymer-based artificial cells with the ability to express proteins. They are created by biocatalytic atom transfer radical polymerization-induced self-assembly (bioPISA). The metalloprotein myoglobin synthesises amphiphilic block copolymers that self-assemble into structures ranging from micelles over worm-like micelles to polymersomes and giant unilamellar vesicles (GUVs). The GUVs encapsulate cargo during the polymerisation, including enzymes, nanoparticles, microparticles, plasmids and cell lysate. The resulting artificial cells act as microreactors for enzymatic reactions and for osteoblast-inspired biomineralization, and could express proteins when fed with amino acids, as shown by the expression of the fluorescent protein mClover and of actin. Actin polymerises in the vesicles and alters the artificial cell's internal structure by creating internal compartments. Thus, bioPISA-derived GUVs mimic bacteria as they are composed of a microscopic reaction compartment that contains genetic information which is able to express proteins upon induction. bioPISA not only is a powerful tool in the pursuit of artificial cells but also for the easy and highly efficient encapsulation of biological molecules under mild conditions and in biologically relevant media. Therefore, it could have significant implications for the development of biomaterials and drug-delivery systems, as well as for cell encapsulation, and the in-situ formation of nano-objects.

INTRODUCTION

The ability to imitate life formation processes holds exciting potential for understanding and controlling biological functions and addressing questions about the origins of life.[1-4] Creating a fully artificial cell remains a significant challenge; however, researchers have made substantial progress in emulating various aspects of living systems, such as cell-like structures,[5-7] growth and replication,[8,9] communication,[10,11] responsiveness,[12-14] protein expression,[12-14] and enzymatic activity.[13,15] Moreover, artificial compartments have been previously used for TX-TL studies.[16] Biomimetic compartment structures are essential components of artificial cells and include polymersomes, liposomes, coacervates, colloidosomes, virus-like particles, and protein cages.[17-22] In particular polymersomes have attracted a lot of attention because they have significant advantages over non-polymer-based self-assemblies, including higher stability. Moreover, the chemical versatility of polymers can be leveraged to design polymersomes with multiple molecular functionalities such as degradability, stability, permeability and stimulus-responsiveness.[14,23-29] Most bottom-up approaches to synthesize polymersomes have limitations due to the complexity of the preparation methodology or because of the low encapsulation efficiency of functional cargo. To address these limitations, researchers have turned to polymerization-induced self-assembly (PISA) as

an effective method to produce polymer-based biomimetic structures, including polymersomes.[26,30,31] PISA involves synthesizing amphiphilic block copolymers in aqueous solution by polymerizing a water-soluble monomer into a water-insoluble polymer block, using a hydrophilic polymeric initiator or chain transfer agent (CTA) for the hydrophilic block. During the initial phase of polymerization, the forming amphiphilic block copolymer is still soluble in water. Once the hydrophobic block has reached a certain length, the copolymers self-assemble. The hydrophobic block continues to grow in length so that the hydrophilic-to-hydrophobic ratio of the block copolymer decreases, and as a result, the morphology of the self-assembled structures evolves from micelles, over worm-like micelles, into vesicles. PISA is usually conducted with reversible-deactivation radical polymerizations (RDRPs), most prominently with reversible addition-fragmentation chain-transfer (RAFT) polymerisations,[26,31-34] but also with atom transfer radical polymerizations (ATRP).[35] PISA works under concentrated reagents conditions, resulting in high concentrations of self-assembled objects, and it allows highly efficient encapsulation of cargo in aqueous solutions in a one-pot procedure.[26,32-34] Recently, PISA has been employed in the synthesis of biomimetic structures such as giant vesicles (GUVs) and polymersome nanoreactors, demonstrating the potential of this technique in the pursuit of artificial cells.[24,31,36-39]

Incorporating biological molecules in artificial cells requires biocompatible conditions, with PISA holding an advantage as it occurs in aqueous solutions. However, initiation conditions can potentially harm sensitive biological molecules. For instance, the high temperatures required for thermal initiators are not ideal when working with biomolecules. Light-triggered polymerisations are safer, especially when visible light is used, but biologically derived initiation may be ideal. An elegant approach would be to use biocatalytic initiation of RDRP systems.[40] Recently, an enzyme-initiated PISA was reported by Tan and coworkers, which employed horse radish peroxidase (HRP) to initiate RAFT polymerisation.[41,42] However, this approach necessitates hydrogen peroxide and the formation of free radicals to initiate the reaction, which could lead to cytoxicity.[43] Moreover, the use of biologically relevant buffers as solvent led to unstable nanoparticles and as such deionised water was employed. Therefore, a more robust bioPISA technique is needed to couple the synthesis and self-assembly of polymers through PISA with biological or bio-mimetic systems. Biocatalytic ATRP (bioATRP) uses enzymes or their cofactors to initiate and control radical polymerisations and was introduced simultaneously by our group[40,44,45] and di Lena and co-workers.[46,47] A wide range of biologically derived catalysts have been employed as ATRPase, such as horseradish peroxidase,[44] laccase,[46] catalase,[47] haemoglobin (Hb),[45,48,49] and myoglobin (Mb).[50] This paves the way for a biocatalytic PISA methodology based on enzyme-mediated ATRP (**Figure 1a**).

Connecting the worlds of bio-polymerizations and life mimesis, here we report the development of biocatalytic polymerization-induced self-assembly (bioPISA) and its application as a bio-compatible methodology to synthesise synthetic cell-like structures. The scope of conditions for bioPISA was investigated, demonstrating its robustness in different media useful for biological applications. To achieve biomimetic systems, different enzymes were encapsulated in GUV synthesised by bioPISA, acting as microreactors, thus showing that the activity of the encapsulated enzymes was retained. Other proteins were instead used to trigger the formation of cytoskeleton-like structures and for osteoblast-inspired biomineralisation. Moreover, as PISA achieves high encapsulation efficiencies, it is well-suited for the creation of complex cell mimics. Thus, bacterial cell lysate and different plasmids were encapsulated inside the GUVs, effectively reconstituting a functional cytoplasm with a simplified chromosome within an artificial cell membrane. The resulting artificial cells were capable of expressing several proteins, which were, in turn, used to alter the artificial cell's internal structure.

RESULTS AND DISCUSSION

Biocatalytic polymerisation-induced self-assembly

The bioPISA procedure was developed with biocompatibility and ease of use in mind. As such, we selected biocompatible chemicals according to the principles delineated by Matyjaszewski and coworkers,[51] and the reaction steps were simplified as much as possible. Mb was selected as biocatalyst because it is a small, robust and unimeric protein that functions as ATRPase at a biologically relevant pH of 7.4 (**Figure 1b**), unlike Hb which requires acidic pH to become an ATRPase.[45,48] Moreover, Mb also displays peroxidase activity,[52] which is of

relevance for the preparation of enzymatically active self-assemblies, as discussed below. In a typical bioPISA, the hydrophilic macromolecular ATRP initiator poly(ethylene glycol) methyl ether 2-bromoisobutyrate (mPEG-BiB) was chain-extended with 2-hydroxypropyl methacrylate (HPMA), which is the most commonly used monomer for PISA.[26] The reaction was carried out in a phosphate buffer solution at pH 7.4 with 100 mM of NaBr (PBS-Br) containing 5 v/v% DMSO, myoglobin (Mb) and the reducing agent sodium ascorbate (NaAsc) at 37 °C (**Figure 1c**). The monomer concentration was varied between 10 wt% and 25 wt%, and various degree of polymerizations (DP) were targeted by adjusting the initiator:monomer ratio between 150 and 400 (**Figure S1**). The reactions were run for 4 h before they were stopped by opening the reaction mixtures to air. The formation of nanostructures was easily recognised with the naked eye as after 1 h the reaction mixtures were already opaque (**Figure S2**). ^{1}H NMR spectroscopy showed that after less than 2 h the monomer consumption usually plateaued, indicating the end of the reaction (**Figure S3**). Moreover, kinetic data displayed the characteristic shape for a PISA process with a hastening of the monomer consumption at the onset of aggregation (**Figure S4**).[33] The Mb-mediated PISA proceeded faster than Mb-catalysed ATRP in solution, as PISA conditions compared to conventional solution polymerisation often lead to high monomer consumption in shorter reaction time.[53,54] When a monomer concentrations of >10 wt% was used in the reactions, the final monomer consumption, except for high DP and lower wt% conditions, exceeded 90% which indicated near complete conversion (**Table S1**). In contrast, when a lower concentration of monomer was employed (5 wt%), a lower monomer consumption occured (< 60%). At the same time, the reaction for high DPs (*i.e.* lower initiator concentration) also yielded low monomer consumption which established that a certain threshold of monomer and initiator concentration was necessary for the reaction to reach high yields. bioPISA from a small molecule initiator (2-hydroxyethyl 2-bromoisobutyrate) led to the formation of a macroscopic precipitation. This is certainly a consequence of the absence of mPEG as hydrophilic block in the forming polymers, which acts as stabilising hydrophilic corona for the forming self-assemblies.
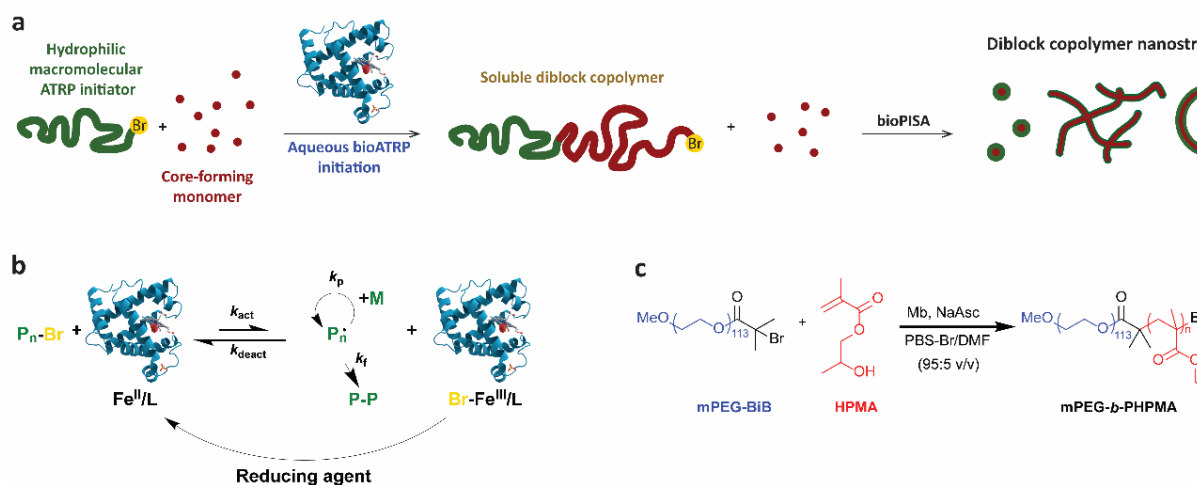

Figure 1. a) Scheme of the bioPISA process that produces various self-assembled structures in aqueous solutions. b) Mechanism of Mb-mediated bioATRP. c) Reaction scheme of bioPISA by chain-extension of a PEG-BiB macroinitiator with HPMA in aqueous solution resulting in the amphiphilic diblock copolymer mPEG-*b*-PHPMA.

One of the key features of PISA is that it allows to tailor the morphology of the resulting structures by varying parameters such as the degree of polymerisation (DP) of either block or the monomer concentration in the reaction mixture.[26,31,32] The case of bioPISA is no different, as the aimed DP of polyHPMA and the concentration of monomer had a clear effect on the morphology, as analysed by transmission electron microscopy (TEM) and dynamic light scattering (DLS). These characterisations allowed to establish a phase diagram representing the morphology of the self-assembled structures as a function of the aimed DP and the initial monomer concentration (**Figure 2** and **Figure S5-Figure S8**). Spherical objects with an average diameter of 227 nm, as

determined from TEM, were obtained at DP 150 and 10 wt%. This size was confirmed by DLS analysis with a hydrodynamic diameter (D_h) of 238 ± 22 nm (**Figure S9**). Worm-like micelles were obtained at DP 150 and 200 with ≥15 wt% and 15-20 wt% of monomer, respectively. The worm-like micelles had an average diameter of 73 ±15 nm as measured by TEM. Interestingly and in accordance with what has been reported before for worm-like micelles synthesised by PISA, the reaction mixtures containing worm morphologies thickened and became self-standing gels (**Figure S6**-**Figure S8**).[55] Increasing the DP between 200 and 300, we could observe an intermediate region of mixed structures, between spheres, worms, and proper vesicles (polymersomes), as longer polymers could self-assemble into diverse shapes; however, at even higher DP and lower wt% (above 300 and below 20, respectively), the polymerization yield was <60%, with either mixed or spherical morphologies. Vesicles (polymersomes) were obtained with DPs of 250, to 400 at monomer concentrations of ≥20 wt%. The diameter of the polymersomes ranged from a few hundred nanometres up to several micrometres, as imaged by TEM and confocal laser scanning microscopy (CLSM) (**Figure S10**). This broad range of sizes meant that it was not possible to fully analyse the suspensions by light-scattering. The membrane of the polymersomes is clearly visible in the TEM images with a thickness of 50 ± 11 nm. The micrometre-sized polymersomes are giant unilamellar vesicles (GUVs) and therefore ideally suited as shell of an artificial cell.

All three morphologies were further analysed by cryo-TEM. Similar structures to those imaged by dry-state TEM were found (**Figure S11**). However, the spherical objects showed internal structures resembling spherically entangled worm-like micelles, similar to those reported by Lee *et al.* for mixtures of copolymers with high- and low-molecular weight hydrophobic blocks.[56] The polymersome membrane can also be clearly identified in the cryo-TEM images, and an average thickness of 44 ± 10 nm was measured.
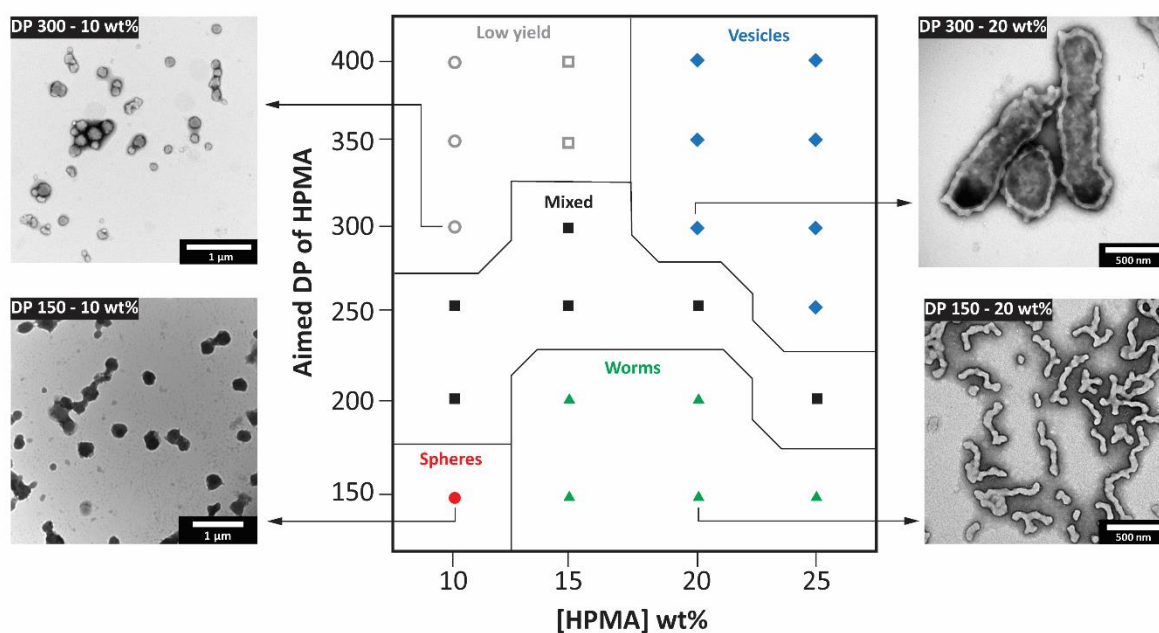

Figure 2. The phase diagram of bioPISA from a PEG-macroinitiator with varying content of HPMA (wt%) and aimed DP of HPMA with illustrating dry state TEM images of the different morphologies. Morphology: sphere (circle), worms (triangle), vesicles (diamond) and mixture (square). Monomer consumption: ≥85% (full symbols) and <85% (empty symbols).

In order to interface bioPISA with biological systems it is important that bioPISA can not only be carried out in simple buffers, but also in complex biological media. To this end, bioPISA was conducted in three different cell culture media: Luria-Bertani (LB), Minimum Essential Medium (MEM) and RPMi-1640, aiming for spheres, worms and vesicles. The reactions yielded high monomer consumption along with self-assemblies of the same morphology and similar sizes as the reactions in PBS-Br (**Figure S9**, **Figure S12**, **Figure S13**, **Figure S14**, and **Table S1**). Moreover, when bioPISA was carried out in the presence of *Escherichia coli*, the bacteria remained viable

(**Figure S15**, **Figure S16**). Taken together, these results prove the robustness of bioPISA to synthesise structures in biologically relevant aqueous solutions and opens the road to an easy, enzyme-catalysed synthesis of self-assemblies for biomaterials, living matter encapsulation or *in situ* formation of biomimetic nano-objects and synthetic cells. As GUVs are the required morphology for artificial cells, all further bioPISA experiments were carried out under conditions targeting a DP of 400 and with a monomer concentration of 25 wt% (**Table S2**).

Encapsulation by bioPISA

The first step towards the creation of artificial cells with bioPISA-derived micro-sized vesicles is to mimic the ability of cells to encapsulate macromolecules,[57,58] particles and internal compartments[59] in order to create a complex environment in the lumen of the GUVs. In order to show that bio-PISA vesicles can encapsulate compounds with a range of different sizes, bioPISA reactions were run in the presence of 40 kDa FITC-labelled dextran, β-galactosidase (β-gal; 102 kDa), and fluorescent silica nanoparticles (Alexa405 SiO_2 NP). The encapsulation efficiency (EE) of these cargoes, along with Mb that self-encapsulates, was ~85% for Mb, and decreased with the increase of the species' R_h to 60% for the silica nanoparticles (Figure 3**a**). CLSM imaging, which is limited by its resolution to the GUVs present in the mixture, showed that each of the fluorescent species was encapsulated into the GUVs (**Figure 3b-c**). Even fluorescent polystyrene microparticles (PS-µP FITC, **Figure 3d**) could be encapsulated, but they tended to clump together during bioPISA, some vesicles to be empty, and some to contain several particles. It should be noted that the GUV membrane was confirmed to be impermeable for macromolecules (**Figure S17**, **Figure S18**), so that the GUVs would not lose their cargo once the vesicles have formed in bioPISA. The reaction also showed good compatibility with living cells (**Figure S15, Figure S16**) and monomer consumption remained high regardless of the cargo in the reaction mixture, including bacteria (**Figure S19**).
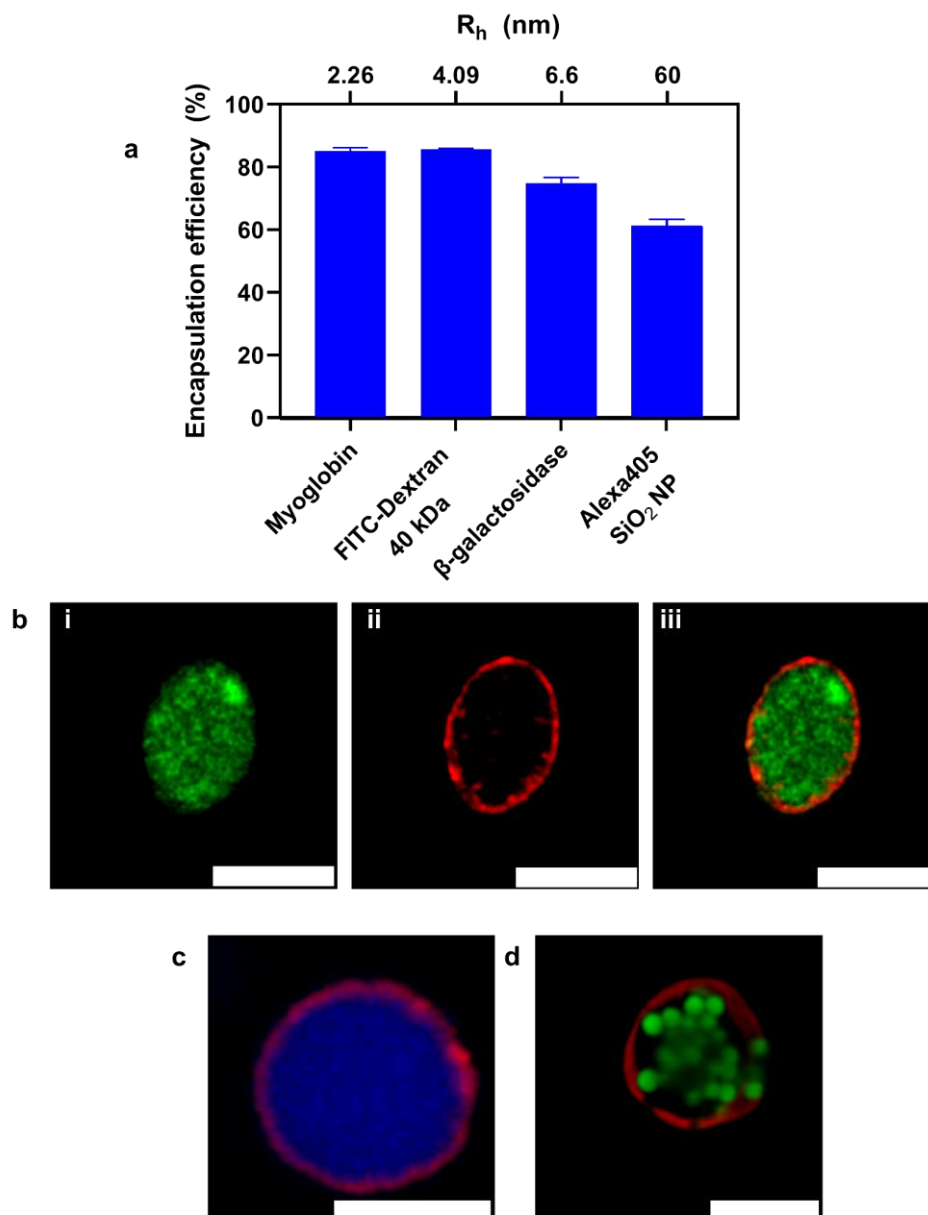
Figure 3. Encapsulation of biomacromolecules, nanoparticles and microparticles into polymersomes by bioPISA. a) Encapsulation efficiency for enzymes, dextran and silica nanoparticles by bioPISA as measured by UV-vis and fluorimetry (values as mean ± SD, n= 3 replicates; R_h measured via DLS for the SiO$_2$ NPs, obtained from the literature for other species). b) CLSM micrographs of a FITC-Dextran 40 kDa-loaded GUV: i) FITC-Dextran 40 kDa ii) Cy5-PEG$_{3.5k}$-cholesterol membrane stain iii) overlay. Scalebar: 5 μm. c) Overlay CLSM micrograph of Alexa405 SiO$_2$NP-loaded GUVs (blue: nanoparticles, red: Cy5-PEG$_{3.5k}$-cholesterol). Scalebar: 5 μm d) CLSM 3D section of a GUV harbouring PS-μP FITC, with microparticles clumping together inside of the GUV (green: microparticles, red: Cy5-PEG$_{3.5k}$-cholesterol). Scalebar: 10 μm. General reaction conditions: [HPMA] 20 wt%, aimed DP: 400.

bio-PISA GUVs as microreactors for encapsulated enzymes

The second fundamental feature for a cell-like system is the presence of a metabolism, that is the ability to perform localized chemical reactions, as both real and synthetic cells are effectively microreactors.[60,61] This generally requires catalysts, where enzymes play this role in biological settings, able to conduct the required reactions in the cells. Even without the encapsulation of an additional enzyme, the bioPISA-derived GUVs are microreactor themselves as they host Mb that self-encapsulates during the PISA process. The capability of

encapsulated Mb to transform the substrate Amplex Red (AR) into the fluorescent resorufin in the presence of H_2O_2 was monitored (**Figure 4a**). Fluorescence increased over time, indicating that the Mb is active inside of the polymersomes and that the polymersome membrane is permeable for the small molecule substrates. The latter observation is in line with previous studies that showed that PISA-derived mPEG-*b*-PHPMA vesicle membranes are permeable for small water-soluble compounds, but impermeable for macromolecules.[15] At the same enzyme concentration, encapsulated Mb exhibited a lower activity than free Mb (246 RFU/minute vs 18000 RFU/minute) (**Figure 4b**). The decrease in specific activity might be a consequence of the slow diffusion of the substrate across the membrane,[62] although it cannot be ruled out that some of the enzyme is irreversibly deactivated. The barrier effect of the membrane was also confirmed in CLSM, where fluorescence was visible only within the lumen of GUVs (**Figure 4c**).

Real cells are complex systems where the various constituents interact in different ways such as regulation feedback and cascade reactions. The next step for the bioPISA GUVs towards artificial cells was to co-encapsulate enzymes acting in parallel to Mb but with an orthogonal activity (Figure 4**d**). β-Galactosidase (β-gal) is a robust, widely used enzyme for industrial biotransformations and prodrug activation,[63,64] and was an ideal candidate as it does not interfere with Mb activity. Similarly to Mb, β-gal activity (the hydrolysis of fluorescein di-β-D-galactopyranoside, FDG) was lower in the vesicles than for free enzyme (36 vs. 1730 RFU/minute), which could be due to a certain level of deactivation during the bioPISA, or more likely, due to diffusion limitation by the membrane (Figure 4**e**), the latter hypothesis being supported by the observation that the resulting fluorescein concentrated within the lumen of the GUVs (Figure 4**f**). Finally, a glucose oxidase (GOx) – Mb enzyme cascade[65] was established in the GUVs where the formation of the final product requires the synergy of two co-encapsulated enzymes (Figure 4**g**). Driven by the GOx-catalysed reaction of glucose and oxygen into glucono-1,5-lactone and H_2O_2, followed by a peroxidase reaction catalysed by Mb, the cascade led to the production of resorufin in the bioPISA-derived GUVs (Figure 4**h**). Thus, the bioPISA GUVs served as microreactors for enzyme cascades and were able to develop both fluorescence based on the substrates provided.
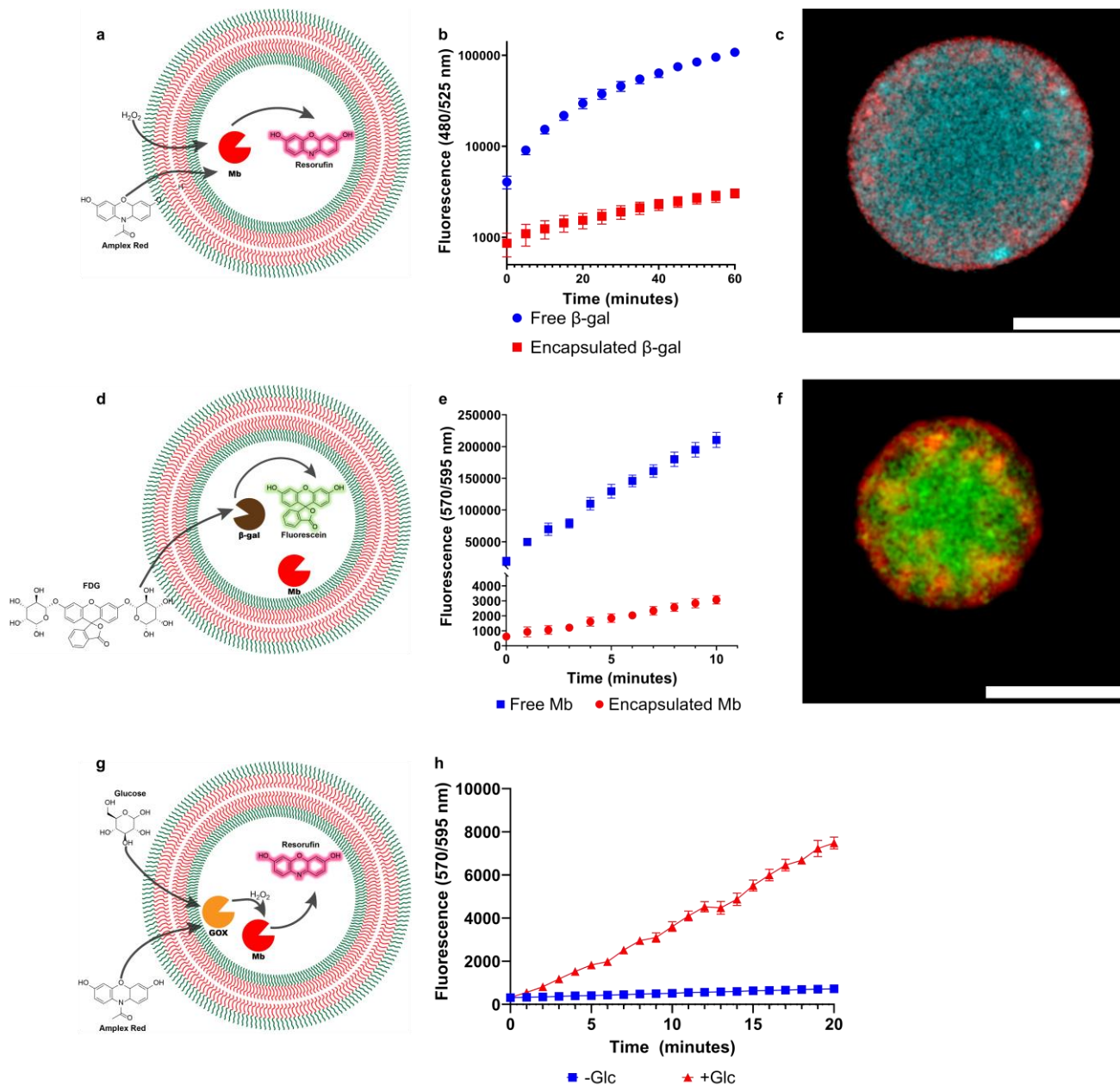
Figure 4. bioPISA-derived GUVs as microreactors for enzymes. a) Scheme of a 1-enzyme microreactor, producing fluorescence from external substrates. b) Peroxidase activity of encapsulated and free Mb with H_2O_2 and AR. c) CLSM micrograph of a Mb-containing GUV after the reaction (cyan: resorufin, red: Cy5-PEG$_{3.5k}$-cholesterol). d) Scheme of an artificial cell with two co-encapsulated enzymes, producing fluorescence from external substrates. e) Hydrolase activity of encapsulated and free β-gal with FDG. f) CLSM micrograph of a β-gal+Mb-containing GUV after the reaction (green: fluorescein, red: Cy5-PEG$_{3.5k}$-cholesterol). g) Scheme of an artificial cell with two co-encapsulated enzymes producing fluorescence from external substrates following a cascade reaction. h) Peroxidase activity of encapsulated GOx+Mb cascade with AR. All values displayed as mean ± SD, n = 3 replicates for all experiments. Scalebars for all images: 5 μm.

Triggered structure modifications in bioPISA GUVs

A third characteristic of cells is their ability to respond to external stimuli, for instance by altering their shape and structure.[66] Several kinds of stimuli-responsive artificial cells have been designed in the past,[67,68] including polymer-based structures that change their shape upon a specific external trigger,[69-72] but so far none can compete with actual cells in complexity.

8

An example of such structural complexity is the formation of cytoskeleton-like structures. The cytoskeleton component actin is known to produce tight, stiff networks together with the crosslinker filamin, once it polymerizes from G-actin to F-actin at high Mg^{2+} concentrations.[73-75] Using bioPISA to encapsulate filamin and fluorescently-labelled actin, we observed magnesium-triggered changes in GUVs' internal architecture (**Figure 5a).** This led to subcompartmentalized vesicles with condensed actin, resembling a hybrid of PDMS-PMOXA GUVs encapsulating actin (which can form internal vesicles),[73] and actinosomes (which create protein shells around coacervates)[76,77] (**Figure 5b**, **Figure S20**). These structures did not form in absence of Mg^{2+} (**Figure S21**) or without actin (**Figure S22**), confirming that actin polymerization in the confined space of the GUVs let to their formation.

However, many cell types do not rely only on biomolecules to modify their architecture, but can also use minerals to produce matrices and scaffolds,[78] becoming of interest for materials science and architecture as well.[79] A biomineralizing system was developed, where encapsulated alkaline phosphatase (ALP) (**Figure S23**) converted the dissolved calcium glycerophosphate (CaGP) to insoluble calcium phosphate.[80] This precipitation reaction imitated the biological mechanism in which osteoblasts produce the mineral matrix of bones (Figure 5**c**). The reaction produced the expected white precipitate of calcium phosphate only in presence of ALP in the GUV and CaGP (**Figure S24**) added outside. By adsorbing fluorescein to the mineral,[81] the resulting particles could be imaged (**Figure 5d, Figure S25**). Due to the intravesicular localization of ALP, the calcium phosphate precipitated within the GUVs, causing the destabilization of the polymer membrane, which adsorbed on the phosphate particles. Thanks to an encapsulated enzyme, the GUVs could turn into a new organic-inorganic hybrid material, where the biomineral could be wholly contained within the polymer matrix.
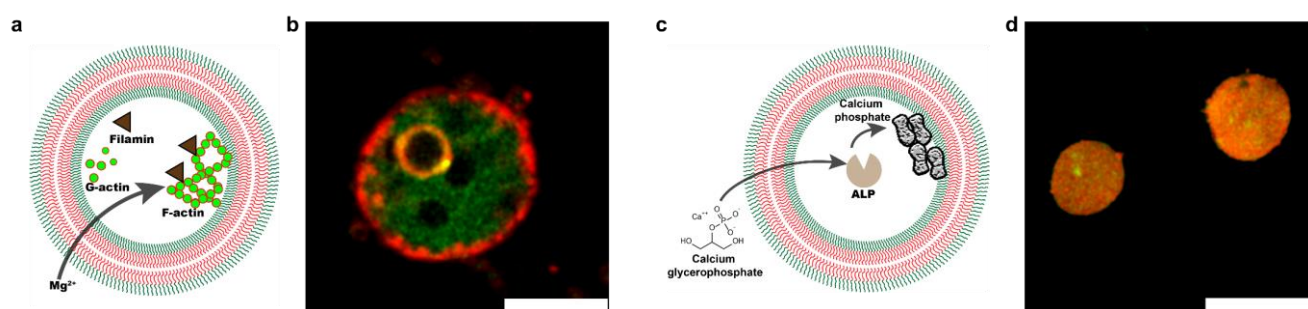

Figure 5. Triggered structure modifications in bioPISA GUVs. a) Scheme of the Mg^{2+}-induced polymerization/condensation of actin in GUVs. b) CLSM micrograph of a GUV after the formation of actin condensates (actin/actin-Atto488/filamin: 1/0.25/0.01 weight ratio; green: actin-Atto488, red: Cy5-PEG$_{3.5k}$-cholesterol; the cholesterol dye could only label some of the inner vesicles). Scalebar: 5 µm. c) Scheme of ALP-mediated calcium phosphate precipitation within GUVs. d) CLSM micrograph of a GUV after the biomineralization of CaGP by ALP, having become a polymer-mineral capsule. Green: calcium phosphate-adsorbed fluorescein. Red: Cy5-PEG3.5k-cholesterol. Scalebar: 10 µm.

bioPISA GUVs as artificial bacteria capable of protein expression

A key feature of cells is their ability to express proteins through the DNA transcription and RNA translation (TX-TL mechanism. Thus, encapsulating cell cytoplasm into bioPISA GUVs could potentially reconstitute this cellular function and turn them into artificial cells. We developed a reaction mixture for bioPISA that contained *E. coli* lysate (S30 extract, containing 25% of the total bacterial proteome[82]) and a plasmid of interest, so that all proteins, ribosomes, tRNAs, and the plasmid were encapsulated into the GUVs. Amino acids (a.a.) were added from the outside to the GUVs, as well as the Premix, containing nucleotides (NTPs), salts, IPTG and pyruvate kinase for ATP regeneration,[16,83] The TX-TL capability of this new system was confirmed with the expression of the fluorescent mClover protein in the bioPISA GUVs (**Figure 6a**), yielding fluorescent vesicles as confirmed by confocal microscopy (**Figure 6b**) and by flow cytometry (**Figure S26**). The semiquantitative analysis of the fluorescence signal over time shows a quick baseline increase once the reaction is started, but the protein

expression can only be sustained on the longer term when both amino acids and the Premix are added to plasmid-containing GUVs, and otherwise can only rely on residual molecules (a.a., NTPs) in the cell lysate.[84,85] These results clearly showed that bioPISA resulted in bacteria-mimetic structures, i.e. microscopic reaction compartments with a single "chromosome" (the plasmid) with no sub-compartmentalization, capable of expressing proteins upon induction.

Cells are also able to modify their internal structure, and need to express specific proteins to that end. As we demonstrated above, the condensation of F-actin produced internal compartments in the GUVs. Intrigued by this phenomenon, actin was expressed in the presence of fluorescently-labelled phalloidin (**Figure 5d**), to promote the polymerization of actin even at low concentrations[86] and allow its visualization. At the same conditions of the pre-encapsulated actin, we could observe actin condensation leading to internal compartments, but with seemingly looser structures than with the former (**Figure 5e, Figure S27**), suggesting once again that the interplay between actin and the membrane induced changes in the GUV structure.

Similarly, ALP was expressed as functional enzyme (**Figure 5f, g, Figure S28**) and induced calcium phosphate precipitation (**Figure S29**). In contrast to the studies above, the enzyme formed calcium phosphate cores inside of the GUVs that in some cases extended and deformed the vesicle membrane so that protrusions formed (**Figure 5h**, **Figure S30**). We speculate that the difference in morphology between GUV-calcium phosphate structures obtained by ALP expressed *in situ* compared to directly encapsulated ALP might be a consequence of a lower concentration of enzyme inside of the GUVs in the former case, causing a lower production of calcium phosphate that then precipitated within the lumen of the vesicles without destabilizing their membranes.

The three examples of protein expression within bioPISA-derived GUVs show that polymer-based artificial cells could be produced by enzymatic polymerization while simultaneously encapsulating the TX-TL machinery which expressed proteins and enzyme that in turn modified the structure of the artificial cells. Thus, these "artificial bacteria" possessed emergent structural properties.
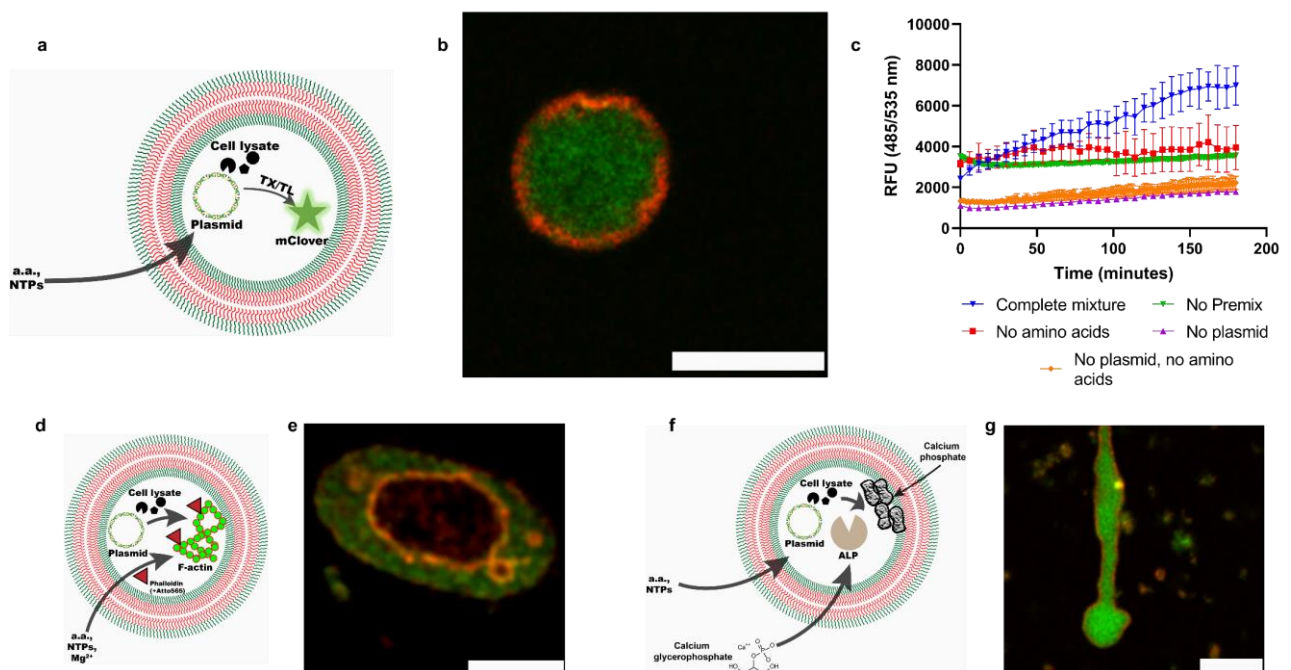

Figure 6. bioPISA GUVs as artificial bacterium capable of protein expression. a) Scheme of cell-free expression of mClover in GUVs, where amino acids and NTPs are provided from the outside to a GUV encapsulating the plasmid and the S30 cell lysate, resulting in the expression of the fluorescent protein. b) CLSM micrograph of a GUV after expression of mClover. Green: mClover. Red: Cy5-PEG3.5k-cholesterol. c) Expression profiles of the fluorescent mClover in GUVs with no plasmid (baseline), plasmid alone or plasmid and amino acids. All values displayed as mean ±SD, n=3 replicates for all experiments. d) Scheme of a GUV containing a plasmid and bacterial translation machinery, producing an actin cytoskeleton. e) CLSM micrograph of a GUV with expressed actin + phalloidin-Atto565 (green: phalloidin-Atto565, red: Cy5-PEG$_{3.5k}$-cholesterol). f) Scheme of a GUV containing a plasmid and bacterial translation machinery for the production of ALP, and subsequent ALP-catalysed

biomineralization of calcium phosphate. g) CLSM micrograph of a GUV after the biomineralization of CaGP by expressed ALP. Green: calcium phosphate-adsorbed fluorescein. Red: Cy5-PEG3.5k-cholesterol. Scalebars for all images: 10 μm.

CONCLUSIONS

In this work, we have demonstrated how an enzymatic reaction can induce the formation of new-to-nature polymeric vesicles, which can be equipped to increasing levels of complexity, from simple vessels to microreactors and full cell mimics capable of producing their own proteins, thanks to the co-encapsulated plasmids as genetic information. For the first time, an enzyme could self-encapsulate within an unnatural membrane it synthesized, entrapping all the complex components deriving from cell lysates, which in turn could express specific proteins and modify the structure of the vesicles, producing internal compartments, or transforming them into polymer-mineral hybrids. Cell mimics were produced in the most bio-similar process possible, showcasing the versatility and robustness of bioCRP. Moreover, bioPISA proved to be a very efficient and biocompatible encapsulation method for a range of cargo. Our findings will pave the way for novel hybrid systems combining synthetic polymers with the diversity of natural molecules, offering a plethora of applications in synthetic biology, sensing, catalysis and biomaterials.

ACKNOWLEDGEMENTS

REFERENCES

1   Otto, S. An Approach to the De Novo Synthesis of Life. *Accounts of Chemical Research* **55**, 145-155, doi:10.1021/acs.accounts.1c00534 (2022).

2   Mann, S. The Origins of Life: Old Problems, New Chemistries. *Angewandte Chemie International Edition* **52**, 155-162, doi:https://doi.org/10.1002/anie.201204968 (2013).

3   Del Bianco, C. & Mansy, S. S. Nonreplicating Protocells. *Accounts of Chemical Research* **45**, 2125-2130, doi:10.1021/ar300097w (2012).

4   Xu, C., Hu, S. & Chen, X. Artificial cells: from basic science to applications. *Materials Today* **19**, 516-532, doi:https://doi.org/10.1016/j.mattod.2016.02.020 (2016).

5   Kumar, S., Karmacharya, M. & Cho, Y.-K. Bridging the Gap between Nonliving Matter and Cellular Life. *Small* **n/a**, 2202962, doi:https://doi.org/10.1002/smll.202202962 (2022).

6   Guindani, C., da Silva, L. C., Cao, S., Ivanov, T. & Landfester, K. Synthetic Cells: From Simple Bio-Inspired Modules to Sophisticated Integrated Systems. *Angewandte Chemie International Edition* **61**, e202110855, doi:https://doi.org/10.1002/anie.202110855 (2022).

7   Buddingh', B. C. & van Hest, J. C. M. Artificial Cells: Synthetic Compartments with Life-like Functionality and Adaptivity. *Accounts of Chemical Research* **50**, 769-777, doi:10.1021/acs.accounts.6b00512 (2017).

8   Maity, S. *et al.* Caught in the Act: Mechanistic Insight into Supramolecular Polymerization-Driven Self-Replication from Real-Time Visualization. *Journal of the American Chemical Society* **142**, 13709-13717, doi:10.1021/jacs.0c02635 (2020).

9   Zwicker, D., Seyboldt, R., Weber, C. A., Hyman, A. A. & Jülicher, F. Growth and division of active droplets provides a model for protocells. *Nature Physics* **13**, 408-413, doi:10.1038/nphys3984 (2017).

10   Robinson, A. O., Venero, O. M. & Adamala, K. P. Toward synthetic life: Biomimetic synthetic cell communication. *Current Opinion in Chemical Biology* **64**, 165-173, doi:https://doi.org/10.1016/j.cbpa.2021.08.008 (2021).

11   Niederholtmeyer, H., Chaggan, C. & Devaraj, N. K. Communication and quorum sensing in non-living mimics of eukaryotic cells. *Nature Communications* **9**, 5027, doi:10.1038/s41467-018-07473-7 (2018).

12   Pearce, S. & Perez-Mercader, J. Chemoadaptive Polymeric Assemblies by Integrated Chemical Feedback in Self-Assembled Synthetic Protocells. *ACS Central Science* **7**, 1543-1550, doi:10.1021/acscentsci.1c00681 (2021).

13   Cheng, G. *et al.* Self-Assembly of Smart Multifunctional Hybrid Compartments with Programmable Bioactivity. *Chemistry of Materials* **29**, 2081-2089, doi:10.1021/acs.chemmater.6b04326 (2017).

14   Cheng, G. & Pérez-Mercader, J. Engineering Programmable Synthetic Vesicles with Permeability Regulated by a Single Molecular Bridge. *Chemistry of Materials* **31**, 5691-5698, doi:10.1021/acs.chemmater.9b01635 (2019).

15   Blackman, L. D. *et al.* Permeable Protein-Loaded Polymersome Cascade Nanoreactors by Polymerization-Induced Self-Assembly. *ACS Macro Letters* **6**, 1263-1267, doi:10.1021/acsmacrolett.7b00725 (2017).

16   Caschera, F. & Noireaux, V. Compartmentalization of an all-E. coli Cell-Free Expression System for the Construction of a Minimal Cell. *Artificial Life* **22**, 185-195, doi:10.1162/ARTL_a_00198 (2016).

17   Spoelstra, W. K., Deshpande, S. & Dekker, C. Tailoring the appearance: what will synthetic cells look like? *Current Opinion in Biotechnology* **51**, 47-56, doi:https://doi.org/10.1016/j.copbio.2017.11.005 (2018).

18   Schoonen, L. & van Hest, J. C. M. Compartmentalization Approaches in Soft Matter Science: From Nanoreactor Development to Organelle Mimics. *Advanced Materials* **28**, 1109-1128, doi:https://doi.org/10.1002/adma.201502389 (2016).

19   Marguet, M., Bonduelle, C. & Lecommandoux, S. Multicompartmentalized polymeric systems: towards biomimetic cellular structure and function. *Chemical Society Reviews* **42**, 512-529, doi:10.1039/c2cs35312a (2013).

20   Rideau, E., Dimova, R., Schwille, P., Wurm, F. R. & Landfester, K. Liposomes and polymersomes: a comparative review towards cell mimicking. *Chemical Society Reviews* **47**, 8572-8610, doi:10.1039/C8CS00162F (2018).

21   Gouveia, M. G. *et al.* Polymersome-based protein drug delivery – quo vadis? *Chemical Society Reviews* **52**, 728-778, doi:10.1039/D2CS00106C (2023).

22   Rother, M., Nussbaumer, M. G., Renggli, K. & Bruns, N. Protein cages and synthetic polymers: a fruitful symbiosis for drug delivery applications, bionanotechnology and materials science. *Chemical Society Reviews* **45**, 6213-6249, doi:10.1039/C6CS00177G (2016).

23   Matoori, S. & Leroux, J.-C. Twenty-five years of polymersomes: lost in translation? *Materials Horizons* **7**, 1297-1309, doi:10.1039/C9MH01669D (2020).

24   Varlas, S. *et al.* Tuning the membrane permeability of polymersome nanoreactors developed by aqueous emulsion polymerization-induced self-assembly. *Nanoscale* **11**, 12643-12654, doi:10.1039/C9NR02507C (2019).

25   Pei, Y., Lowe, A. B. & Roth, P. J. Stimulus-Responsive Nanoparticles and Associated (Reversible) Polymorphism via Polymerization Induced Self-assembly (PISA). *Macromolecular Rapid Communications* **38**, 1600528, doi:https://doi.org/10.1002/marc.201600528 (2017).

26   Penfold, N. J. W., Yeow, J., Boyer, C. & Armes, S. P. Emerging Trends in Polymerization-Induced Self-Assembly. *ACS Macro Letters* **8**, 1029-1054, doi:10.1021/acsmacrolett.9b00464 (2019).

27   Busatto, N., Stolojan, V., Shaw, M., Keddie, J. L. & Roth, P. J. Reactive Polymorphic Nanoparticles: Preparation via Polymerization-Induced Self-Assembly and Postsynthesis Thiol–para-Fluoro Core Modification. *Macromolecular Rapid Communications* **40**, 1800346, doi:https://doi.org/10.1002/marc.201800346 (2019).

28   Sobotta, F. H. *et al.* Tuneable Time Delay in the Burst Release from Oxidation-Sensitive Polymersomes Made by PISA. *Angew Chem Int Ed Engl*, https://doi.org/10.1002/anie.202108928, doi:10.1002/anie.202108928 (2021).

29   Le, D., Keller, D. & Delaittre, G. Reactive and Functional Nanoobjects by Polymerization-Induced Self-Assembly. *Macromolecular Rapid Communications* **40**, 1800551, doi:https://doi.org/10.1002/marc.201800551 (2019).

30   Cheng, G. & Pérez-Mercader, J. Polymerization-Induced Self-Assembly for Artificial Biology: Opportunities and Challenges. *Macromolecular Rapid Communications* **40**, 1970006, doi:https://doi.org/10.1002/marc.201970006 (2019).

31   Wan, J., Fan, B. & Thang, S. H. RAFT-mediated polymerization-induced self-assembly (RAFT-PISA): current status and future directions. *Chemical Science* **13**, 4192-4224, doi:10.1039/D2SC00762B (2022).

32   D'Agosto, F., Rieger, J. & Lansalot, M. RAFT-Mediated Polymerization-Induced Self-Assembly. *Angewandte Chemie International Edition* **59**, 8368-8392, doi:https://doi.org/10.1002/anie.201911758 (2020).

33   Charleux, B., Delaittre, G., Rieger, J. & D'Agosto, F. Polymerization-Induced Self-Assembly: From Soluble Macromolecules to Block Copolymer Nano-Objects in One Step. *Macromolecules* **45**, 6753-6765, doi:10.1021/ma300713f (2012).

34   Lansalot, M. & Rieger, J. Polymerization-Induced Self-Assembly. *Macromolecular Rapid Communications* **40**, 1800885, doi:https://doi.org/10.1002/marc.201800885 (2019).

35   Liu, C., Hong, C. Y. & Pan, C. Y. Polymerization techniques in polymerization-induced self-assembly (PISA). *Polym Chem-Uk* **11**, 3673-3689, doi:10.1039/d0py00455c (2020).

36   Bastakoti, B. P. & Perez-Mercader, J. Facile One-Pot Synthesis of Functional Giant Polymeric Vesicles Controlled by Oscillatory Chemistry. *Angewandte Chemie International Edition* **56**, 12086-12091, doi:https://doi.org/10.1002/anie.201703816 (2017).

37   Yoshida, E. Giant vesicles prepared by nitroxide-mediated photo-controlled/living radical polymerization-induced self-assembly. *Colloid and Polymer Science* **291**, 2733-2739, doi:10.1007/s00396-013-3056-0 (2013).

38   Yoshida, E. Morphology control of giant vesicles by manipulating hydrophobic-hydrophilic balance of amphiphilic random block copolymers through polymerization-induced self-assembly. *Colloid and Polymer Science* **292**, 763-769, doi:10.1007/s00396-013-3154-z (2014).

39   Albertsen, A. N., Szymański, J. K. & Pérez-Mercader, J. Emergent Properties of Giant Vesicles Formed by a Polymerization-Induced Self-Assembly (PISA) Reaction. *Scientific Reports* **7**, 41534, doi:10.1038/srep41534 (2017).

40   Rodriguez, K. J. *et al.* Repurposing Biocatalysts to Control Radical Polymerizations. *ACS Macro Letters* **7**, 1111-1119, doi:10.1021/acsmacrolett.8b00561 (2018).

41   Tan, J. *et al.* Enzyme-PISA: An Efficient Method for Preparing Well-Defined Polymer Nano-Objects under Mild Conditions. *Macromolecular Rapid Communications* **39**, 1700871, doi:doi:10.1002/marc.201700871 (2018).

42   Xu, Q. *et al.* Enzyme catalysis-induced RAFT polymerization in water for the preparation of epoxy-functionalized triblock copolymer vesicles. *Polym. Chem.* **9**, 4908-4916, doi:10.1039/C8PY01053F (2018).

43   Fujisawa, S. *et al.* Radical generation, radical-scavenging activity, and cytotoxicity of eugenol-related compounds. *In vitro & molecular toxicology* **13**, 269-280 (2000).

44   Sigg, S. J. *et al.* Horseradish Peroxidase as a Catalyst for Atom Transfer Radical Polymerization. **32**, 1710-1715, doi:https://doi.org/10.1002/marc.201100349 (2011).

45   Silva, T. B. *et al.* Hemoglobin and Red Blood Cells Catalyze Atom Transfer Radical Polymerization. *Biomacromolecules* **14**, 2703-2712, doi:10.1021/bm400556x (2013).

46   Ng, Y.-H., di Lena, F. & Chai, C. L. L. Metalloenzymatic radical polymerization using alkyl halides as initiators. *Polym Chem-Uk* **2**, 589-594, doi:10.1039/C0PY00139B (2011).

47   Ng, Y.-H., di Lena, F. & Chai, C. L. L. PolyPEGA with predetermined molecular weights from enzyme-mediated radical polymerization in water. *Chemical Communications* **47**, 6464-6466, doi:10.1039/C1CC10989H (2011).

48   Divandari, M., Pollard, J., Dehghani, E., Bruns, N. & Benetti, E. M. Controlling Enzymatic Polymerization from Surfaces with Switchable Bioaffinity. *Biomacromolecules* **18**, 4261-4270, doi:10.1021/acs.biomac.7b01313 (2017).

49   Pollard, J. *et al.* Biocatalytically Initiated Precipitation Atom Transfer Radical Polymerization (ATRP) as a Quantitative Method for Hemoglobin Detection in Biological Fluids. *Analytical Chemistry* **92**, 1162-1170, doi:10.1021/acs.analchem.9b04290 (2020).

50   Hajizadeh, S., Bülow, L. & Ye, L. Synthesizing a Hybrid Nanocomposite as an Affinity Adsorbent through Surface-Initiated Atom Transfer Radical Polymerization Catalyzed by Myoglobin. *ACS Omega* **6**, 10462-10474, doi:10.1021/acsomega.1c00955 (2021).

51   Dworakowska, S., Lorandi, F., Gorczyński, A. & Matyjaszewski, K. Toward Green Atom Transfer Radical Polymerization: Current Status and Future Challenges. **9**, 2106076, doi:https://doi.org/10.1002/advs.202106076 (2022).

52   Guo, C. *et al.* Peroxidase Activity of Myoglobin Variants Reconstituted with Artificial Cofactors. *ChemBioChem* **23**, e202200197, doi:https://doi.org/10.1002/cbic.202200197 (2022).

53   Blanazs, A., Madsen, J., Battaglia, G., Ryan, A. J. & Armes, S. P. Mechanistic Insights for Block Copolymer Morphologies: How Do Worms Form Vesicles? *Journal of the American Chemical Society* **133**, 16581-16587, doi:10.1021/ja206301a (2011).

54   Chaduc, I. *et al.* Batch Emulsion Polymerization Mediated by Poly(methacrylic acid) MacroRAFT Agents: One-Pot Synthesis of Self-Stabilized Particles. *Macromolecules* **45**, 5881-5893, doi:10.1021/ma300875y (2012).

55   Yeow, J., Xu, J. & Boyer, C. Facile Synthesis of Worm-like Micelles by Visible Light Mediated Dispersion Polymerization Using Photoredox Catalyst. *Journal of visualized experiments : JoVE*, doi:10.3791/54269 (2016).

56   Lee, S. J., Cho, A. & Kim, K. T. Morphological Diversity from the Solution Self-Assembly of Block Copolymer Blends Containing High Molecular-Weight Hydrophobic Blocks. *Macromolecular Rapid Communications* **43**, 2100893, doi:https://doi.org/10.1002/marc.202100893 (2022).

57   Seo, H. & Lee, H. Recent developments in microfluidic synthesis of artificial cell-like polymersomes and liposomes for functional bioreactors. *Biomicrofluidics* **15**, 021301, doi:10.1063/5.0048441 (2021).

58   Emir Diltemiz, S. *et al.* Use of artificial cells as drug carriers. *Materials Chemistry Frontiers* **5**, 6672-6692, doi:10.1039/D1QM00717C (2021).

59   Altamura, E., Albanese, P., Mavelli, F. & Stano, P. The Rise of the Nested Multicompartment Model in Synthetic Cell Research. **8**, doi:10.3389/fmolb.2021.750576 (2021).

60   Elani, Y. Interfacing Living and Synthetic Cells as an Emerging Frontier in Synthetic Biology. *Angew. Chem. Int. Ed.* **60**, 5602-5611, doi:https://doi.org/10.1002/anie.202006941 (2021).

61   Belluati, A., Craciun, I., Meyer, C. E., Rigo, S. & Palivan, C. G. Enzymatic reactions in polymeric compartments: nanotechnology meets nature. *Current Opinion in Biotechnology* **60**, 53-62, doi:https://doi.org/10.1016/j.copbio.2018.12.011 (2019).

62   Belluati, A., Craciun, I., Liu, J. & Palivan, C. G. Nanoscale Enzymatic Compartments in Tandem Support Cascade Reactions in Vitro. *Biomacromolecules* **19**, 4023-4033, doi:10.1021/acs.biomac.8b01019 (2018).

63   Vera, C., Guerrero, C., Aburto, C., Cordova, A. & Illanes, A. Conventional and non-conventional applications of β-galactosidases. *Biochimica et Biophysica Acta (BBA) - Proteins and Proteomics* **1868**, 140271, doi:https://doi.org/10.1016/j.bbapap.2019.140271 (2020).

64   Yang, Y.-h., Aloysius, H., Inoyama, D., Chen, Y. & Hu, L.-q. Enzyme-mediated hydrolytic activation of prodrugs. *Acta Pharmaceutica Sinica B* **1**, 143-159, doi:https://doi.org/10.1016/j.apsb.2011.08.001 (2011).

65   Kelman, D. J., DeGray, J. A. & Mason, R. P. Reaction of myoglobin with hydrogen peroxide forms a peroxyl radical which oxidizes substrates. *Journal of Biological Chemistry* **269**, 7458-7463, doi:https://doi.org/10.1016/S0021-9258(17)37308-8 (1994).

66   Janmey, P. A. & McCulloch, C. A. Cell Mechanics: Integrating Cell Responses to Mechanical Stimuli. *Annual Review of Biomedical Engineering* **9**, 1-34, doi:10.1146/annurev.bioeng.9.060906.151927 (2007).

67   Boyd, M. A. & Kamat, N. P. Designing Artificial Cells towards a New Generation of Biosensors. *Trends in Biotechnology* **39**, 927-939, doi:https://doi.org/10.1016/j.tibtech.2020.12.002 (2021).

68   Chakraborty, T. & Wegner, S. V. Cell to Cell Signaling through Light in Artificial Cell Communities: Glowing Predator Lures Prey. *ACS Nano* **15**, 9434-9444, doi:10.1021/acsnano.1c01600 (2021).

69   de Souza Melchiors, M. *et al.* Membrane Manipulation of Giant Unilamellar Polymer Vesicles with a Temperature-Responsive Polymer. *Angewandte Chemie International Edition* **61**, e202207998, doi:https://doi.org/10.1002/anie.202207998 (2022).

70   Ivanov, I. *et al.* Directed Growth of Biomimetic Microcompartments. *Advanced Biosystems* **3**, 1800314, doi:https://doi.org/10.1002/adbi.201800314 (2019).

71   Krishna Kumar, R., Harniman, R. L., Patil, A. J. & Mann, S. Self-transformation and structural reconfiguration in coacervate-based protocells. *Chemical Science* **7**, 5879-5887, doi:10.1039/C6SC00205F (2016).

72   Thamboo, S. *et al.* Mimicking Cellular Signaling Pathways within Synthetic Multicompartment Vesicles with Triggered Enzyme Activity and Induced Ion Channel Recruitment. *Advanced Functional Materials* **29**, 1904267, doi:10.1002/adfm.201904267 (2019).

73   Belluati, A. *et al.* Multicompartment Polymer Vesicles with Artificial Organelles for Signal-Triggered Cascade Reactions Including Cytoskeleton Formation. **30**, 2002949, doi:https://doi.org/10.1002/adfm.202002949 (2020).

74   Ganar, K. A., Honaker, L. W. & Deshpande, S. Shaping synthetic cells through cytoskeleton-condensate-membrane interactions. *Current Opinion in Colloid & Interface Science* **54**, 101459, doi:https://doi.org/10.1016/j.cocis.2021.101459 (2021).

75   Huber, F., Strehle, D. & Käs, J. Counterion-induced formation of regular actin bundle networks. *Soft Matter* **8**, 931-936, doi:10.1039/C1SM06019H (2012).

76   Ganar, K. A., Leijten, L. & Deshpande, S. Actinosomes: Condensate-Templated Containers for Engineering Synthetic Cells. *ACS Synthetic Biology* **11**, 2869-2879, doi:10.1021/acssynbio.2c00290 (2022).

77   Deshpande, S. & Pfohl, T. Real-Time Dynamics of Emerging Actin Networks in Cell-Mimicking Compartments. *PLOS ONE* **10**, e0116521, doi:10.1371/journal.pone.0116521 (2015).

78   Dauphin, Y. A Brief History of Biomineralization Studies. *ACS Biomaterials Science & Engineering*, doi:10.1021/acsbiomaterials.1c01385 (2022).

79   Achal, V., Mukherjee, A., Kumari, D. & Zhang, Q. Biomineralization for sustainable construction – A review of processes and applications. *Earth-Science Reviews* **148**, 1-17, doi:https://doi.org/10.1016/j.earscirev.2015.05.008 (2015).

80   Cosmidis, J. *et al.* Calcium-Phosphate Biomineralization Induced by Alkaline Phosphatase Activity in Escherichia coli: Localization, Kinetics, and Potential Signatures in the Fossil Record. **3**, doi:10.3389/feart.2015.00084 (2015).

81   Sadallah, L., Boukhris, A., Hannache, H. & Gmouh, S. Entrapment of organic fluorophores in calcium phosphate nanoparticles with slow release. *Turkish journal of chemistry* **44**, 142-154, doi:10.3906/kim-1902-57 (2020).

82   Foshag, D. *et al.* The E. coli S30 lysate proteome: A prototype for cell-free protein production. *N Biotechnol* **40**, 245-260, doi:10.1016/j.nbt.2017.09.005 (2018).

83   Garenne, D., Thompson, S., Brisson, A., Khakimzhan, A. & Noireaux, V. The all-E. coliTXTL toolbox 3.0: new capabilities of a cell-free synthetic biology platform. *Synthetic Biology* **6**, ysab017, doi:10.1093/synbio/ysab017 (2021).

84   Fujiwara, K. & Nomura, S.-i. M. Condensation of an Additive-Free Cell Extract to Mimic the Conditions of Live Cells. *PLOS ONE* **8**, e54155, doi:10.1371/journal.pone.0054155 (2013).

85   Pedersen, A., Hellberg, K., Enberg, J. & Karlsson, B. G. Rational improvement of cell-free protein synthesis. *New Biotechnology* **28**, 218-224, doi:https://doi.org/10.1016/j.nbt.2010.06.015 (2011).

86   Koteliansky, V. E., Shartava, A. S., Belkin, A. M., Gneushev, G. N. & Smirnov, V. N. The effects of phalloidin on actin gel-sol transformation. *FEBS letters* **153**, 311-314, doi:10.1016/0014-5793(83)80631-0 (1983).

87   Moreno-Echeverri, A. M. *et al.* Pitfalls in methods to study colocalization of nanoparticles in mouse macrophage lysosomes. *Journal of Nanobiotechnology* **20**, 464, doi:10.1186/s12951-022-01670-9 (2022).

88   Bajar, B. T. *et al.* Improving brightness and photostability of green and red fluorescent proteins for live cell imaging and FRET reporting. *Sci Rep* **6**, 20889, doi:10.1038/srep20889 (2016).

89   Rowan, S. & Cepko, C. L. A POU factor binding site upstream of the Chx10 homeobox gene is required for Chx10 expression in subsets of retinal progenitor cells and bipolar cells. *Developmental biology* **281**, 240-255, doi:10.1016/j.ydbio.2005.02.023 (2005).

90   de Graaf, A. J. *et al.* ATRP, subsequent azide substitution and 'click' chemistry: three reactions using one catalyst in one pot. *Chemical Communications* **47**, 6972-6974, doi:10.1039/C1CC12224J (2011).

91   Belluati, A., Harley, I., Lieberwirth, I. & Bruns, N. *An outer membrane-inspired polymer coating protects and endows E. coli with novel functionalities.* (2022).

92   Gill, S. C. & von Hippel, P. H. Calculation of protein extinction coefficients from amino acid sequence data. *Analytical Biochemistry* **182**, 319-326, doi:https://doi.org/10.1016/0003-2697(89)90602-7 (1989).

93   Teodorescu, M. & Matyjaszewski, K. Atom Transfer Radical Polymerization of (Meth)acrylamides. *Macromolecules* **32**, 4826-4831, doi:10.1021/ma990175x (1999).

94   D'hooge, D. R. *et al.* Assessment of end-group functionality in atom transfer radical polymerization of N-isopropylacrylamide. *European Polymer Journal* **49**, 2344-2355, doi:https://doi.org/10.1016/j.eurpolymj.2013.05.019 (2013).

95   Ribelli, T. G., Lorandi, F., Fantin, M. & Matyjaszewski, K. Atom Transfer Radical Polymerization: Billion Times More Active Catalysts and New Initiation Systems. **40**, 1800616, doi:https://doi.org/10.1002/marc.201800616 (2019).

96   Connell, L. S., Jones, J. R. & Weaver, J. V. M. Transesterification of functional methacrylate monomers during alcoholic copper-catalyzed atom transfer radical polymerization: formation of compositional and architectural side products. *Polymer Chemistry* **3**, 2735-2738, doi:10.1039/C2PY20280H (2012).

97   Save, M., Weaver, J. V. M., Armes, S. P. & McKenna, P. Atom Transfer Radical Polymerization of Hydroxy-Functional Methacrylates at Ambient Temperature: Comparison of Glycerol Monomethacrylate with 2-Hydroxypropyl Methacrylate. *Macromolecules* **35**, 1152-1159, doi:10.1021/ma011541r (2002).

98   Wang, G. *et al.* Polymerization-Induced Self-Assembly (PISA) Using ICAR ATRP at Low Catalyst Concentration. *Macromolecules* **49**, 8605-8615, doi:10.1021/acs.macromol.6b01966 (2016).

99   Khor, S. Y., Truong, N. P., Quinn, J. F., Whittaker, M. R. & Davis, T. P. Polymerization-Induced Self-Assembly: The Effect of End Group and Initiator Concentration on Morphology of Nanoparticles Prepared via RAFT Aqueous Emulsion Polymerization. *ACS Macro Letters* **6**, 1013-1019, doi:10.1021/acsmacrolett.7b00583 (2017).

100   Shetty, S. C. *et al.* Directed Signaling Cascades in Monodisperse Artificial Eukaryotic Cells. *ACS Nano* **15**, 15656-15666, doi:10.1021/acsnano.1c04219 (2021).

101   Shin, Y. *et al.* Spatiotemporal Control of Intracellular Phase Transitions Using Light-Activated optoDroplets. *Cell* **168**, 159-171.e114, doi:10.1016/j.cell.2016.11.054 (2017).

Supporting Information

MATERIALS

Compounds

Polyethylene glycol monomethyl ether (mPEG, 5 kDa), bromoisobutyryl bromide, triethylamine (Et$_3$N), sodium ascorbate (NaAsc), myoglobin (Mb), hydroxypropyl methacrylate (HPMA), Tris-HCl, dimethylformamide (DMF), 4-(dimethylamino)pyridine (≥98%, DMAP), RPMi-1640 (with addition of fetal bovine serum (10%), L-glutamine (1%), penicillin-streptomycin (1%)), FITC-dextran 40kDa, β-galactosidase (β-Gal), glucose oxidase (GOX), alkaline phosphatase (ALP), actin, Atto488 NHS-ester, phalloidin Atto565, calcium glycerophosphate (CaGP), fluorescein di(β-D-galactopyranoside) (FDG), fluorescein diacetate (FDA), and propidium iodide (PI) were purchased from Sigma-Aldrich and used as received. Tetrahydrofurane (THF) and dichloromethane (CH$_2$Cl$_2$) were purchased from Acros Organics. *E. coli* T7 S30 Extract System for Circular DNA was purchased from Promega. All solvents were purchased in high purity. All reactions requiring anhydrous conditions were carried out using dried Schlenk glassware and under inert Ar gas atmosphere. Deuterated solvents were purchased from Cambridge Isotope Laboratories. PBS 10X was prepared and NaBr was added to make PBS-Br 1X (NaBr 100 mM). Alexa405 SiO$_2$ NPs were a gift by Prof. Alke Petri-Fink (Adolphe Merkle Institute, University of Fribourg, Switzerland).[87]

Plasmids

pNCS-mClover3 was a gift from Prof. Markus Biesalski (TU Darmstadt).[88] ZP9 Actin was a gift from Randall Moon (Addgene plasmid # 16932; http://n2t.net/addgene:16932; RRID:Addgene_16932), Chx10 3kb AP (CC#318) was a gift from Connie Cepko (Addgene plasmid # 15205; http://n2t.net/addgene:15205; RRID:Addgene_15205).[89] pNCS-mClover3 was propagated in *E. coli* BL21 (DE3), whereas ZP9A and CHx10 3kbAP were propagated in *E. coli* DH5alpha. All cultures were grown in Luria-Bertani broth supplemented with the antibiotic they would be resistant to (ampicillin or kanamycin) until OD$_{600}$ 1. Then, the plasmids were purified using a QIAprep Spin Miniprep Kit (Qiagen, USA). The amount of purified DNA was quantified at 260 nm using a NanoDrop One/One^C UV-Vis Spectrophotometer (Thermo Scientific).

EXPERIMENTAL PROCEDURES

Synthesis of poly(ethylene glycol) methyl ether 2-bromoisobutyrate (mPEG-BiB)
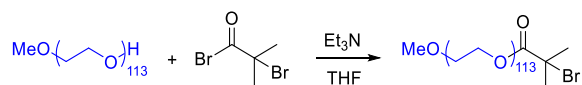
Scheme 1. Synthesis of mPEG-BiB.

mPEG-BiB was synthesised according to a literature procedure.[90] Briefly, mPEG (5000 g mol^{-1}, 2.5 mmol) was dissolved in dry THF (100 mL) under an argon atmosphere and the solution was cooled on ice. Then, triethylamine (0.37 mL, 2.7 mmol, 1.1 eq) was added, followed by 2-bromoisobutyrylbromide (0.33 mL, 2.7 mmol, 1.1 eq). After overnight stirring, the product was filtered. The filtrate was concentrated at reduced pressure and the residue was redissolved in dichloromethane. The product was then isolated by precipitation with diethylether and then dried under vacuum.

BioPISA

Scheme 2. Typical bioPISA reaction.

In a typical bioPISA experiment, HPMA (2 mL, filtered on basic alumina) was measured in a 4 mL vial that was closed with a septum. A certain amount of mPEG-BiB and sodium ascorbate was dissolved in a certain volume PBS-Br buffer pH 7.4 spiked with 5 vol% DMSO in a 4 mL vial closed with a septum. A certain amount of myoglobin was suspended in PBS-Br buffer pH 7.4 in a 10 mL Schlenk flask. All the solutions were degassed with Ar for 1 h. The mPEG-BiB/NaAsc solution was added to the Schlenk flask, and the resulting solution was stirred for 15 min. The colour of the reaction mixture changed from brown to red (myoglobin oxidation). Then, purified HPMA was added. The reaction mixture was stirred for 4 h at room temperature before being opened to air to quench the polymerization by atmospheric oxygen. The final suspension was diluted with 15 mL of PBS. The reagent amounts are specified in **Table S1**. All encapsulations were performed with HPMA 20 wt% and aimed DP 400.

TECHNIQUES

NMR spectroscopy

NMR spectra were recorded on a Bruker Avance III 300 MHz NMR spectrometer (^{1}H NMR 300 MHz) or a Bruker Avance III 400 MHz NMR spectrometer (^{1}H NMR 400 MHz) using deuterated dimethyl sulfoxide (DMSO-d_6) as the solvent. Chemical shifts of protons are reported as δ in parts per million (ppm) and are relative to DMSO-d_6 at δ = 2.54 ppm. Data were evaluated with the MestReNova software suite (v 12.0).

Size exclusion chromatography

To analyse the resulting block copolymers by size exclusion chromatography (SEC), the DP 350, 20 wt% reaction mixtures was centrifuged, and the supernatant removed. The precipitate was diluted in THF. Copolymer samples were prepared as follow: the bioPISA suspension was centrifuged (13000 rpm) and the supernatant was removed. The sample was resuspended in 18 mL DI water, and the purification was repeated 4 times. The remaining residue was let to dry overnight at 40 °C and then suspended in 2 mL THF. The supernatant was passed through a 0.2 μm syringe filter (Whatman® Puradisc 13, PP) before analysis by THF SEC.

SEC experiments were performed on an Agilent 1200 series HPLC system equipped with an Agilent PLgel mixed guard column (particle size= 5 μm) and two Agilent PLgel mixed-D columns (ID = 7.5 mm, L = 300 mm, particle size = 5 μm). Signals were recorded by a UV detector (Agilent 1200 series), an Optilab REX interferometric refractometer, and a miniDawn TREOS light scattering detector (Wyatt Technology Corp.). Samples were run using THF as the eluent at 30 °C and a flow rate of 1.0 mL min^{-1}. Data analyses were carried out on Astra software (Wyatt Technology Corp.) and molecular weights were determined based on narrow molecular weight polystyrene standards calibration (from 540 to 2'210'000 g mol^{-1}).

Dynamic light scattering (DLS)

One drop of the suspension was diluted in deionised water (2 mL). DLS measurements of PISA assemblies were performed on a Zetasizer Nano ZSP (Malvern Instruments, UK) at 25 °C, 173°. Stock solutions were diluted 1:1000 in PBS in a cuvette, with a final volume of 1 mL, measured during 11 runs, repeated three times. Alexa 405-tagged SiO_2 NPs were instead measured according to the same protocol, on a Zetasizer Nano ZS90, at 25°C and 90°. Because of the large size of the polymersomes, only the smaller spherical morphologies were analysed by DLS.

Reaction kinetics

BioPISA reactions were prepared as described and DMSO was replaced by DMF to allow monitoring of the monomer concentration by NMR spectroscopy. Reaction mixtures samples (0.1 mL) were taken at t = 0 and every 10 min and diluted in DMSO-d_6 (0.5 mL) before analysis by ^{1}H NMR spectroscopy.

Confocal laser scanning microscopy (CLSM)

Imaging of vesicles was performed on a Leica SP8 CLSM, equipped with an HCX PL APO 63 × NA 1.2 W CORR CS2 objective (Alexa 405: ex. 405 nm, em. 410 – 430 nm; Fluorescein, mClover, FITC, Atto488: ex. 488 nm, em. 505 – 525 nm; Resorufin, Atto565: ex. 561 nm, em. 570 – 590 nm; Cy5, PI: ex. 635 nm, em. 660 – 690 nm). Membranes were stained with Cy5-PEG$_{3.5k}$-cholesterol, synthesized according to a published procedure.[91] Images were optimized (brightness and contrast; applied evenly throughout a whole image) and analysed via ImageJ. Z-stacks were processed using LAS X software (Leica Camera AG, Germany).

Encapsulation efficiency

Several cargoes were co-encapsulated together with Mb. Depending on the sample, we added to the reaction mixture:

- 32 μL FITC-dextran 40kDa 10 mg ml^{-1}

- 10 μL B-gal 10 mg ml^{-1}

- 10 μL Alexa405 SiO$_2$ NP 1% w/v%

To quantify the encapsulation efficiency, post-polymerization aliquots were diluted 1:10 in PBS, and run through PD 10 desalting columns (Cytvia; gravity protocol) to remove the unencapsulated molecules. The second fraction (7 mL, per supplier's instructions) was recovered as well. Alexa405 SiO$_2$ NP were instead recovered by centrifuging a 1 mL-aliquot of vesicles (500 x g, 3 min, in an Eppendorf microcentrifuge), and recovering the supernatant.

For FITC-dextran and Alexa405 SiO$_2$ NP, a calibration curve was used to quantify the encapsulated fluorophores in the second fraction, on a Clariostar Plus plate reader (BMG Labtech, Germany), in a Greiner transparent 96-well plate.

In the case of Mb, the absorbance at 280 nm in the second fraction was quantified, with ε = 13.98 mM^{-1} cm^{-1}, from its sequence, as of (N of tryptophan residues*5.5) + (N of tyrosine residues*1.5).[92] For β-gal, the protein absorbance at 280 nm was likewise calculated, using the expected content of Mb as blank, with ε= 191.95 mM^{-1} cm^{-1}. The measurements were conducted in a Cary 60 UV-Vis spectrophotometer (Agilent, USA).

FITC-labelled polystyrene microbeads (2 μm diameter) were added to the reaction mixture (10 μL directly from the suspension) and then directly imaged via CLSM.

To quantify unencapsulated Mb after washing of the 1st fraction, the absorbance values after bicinchoninic acid assay (Merck Millipore, protocol according to manufacturer's manual) were compared in GUVs, GUVs after centrifugation (500 x g, 3 min, in an Eppendorf microcentrifuge, 2x) and washing with PBS, and the resulting washing supernatant. Volumes of both GUVs and supernatant were kept constant.

Co-encapsulation of glucose oxidase (GOX)

To obtain GOX-loaded vesicles, GOX was dissolved (1 mg mL^{-1}) together with Mb in the reaction mixture. Then, the vesicles were purified. If needed, samples were incubated 10 minutes in a 1 mg mL^{-1} NaAsc solution before being centrifuged and resuspended (2x) in PBS again.

Enzyme activity of Mb

The enzymatic activity of Mb was measured in a Clariostar Plus plate reader, in a Greiner transparent 96-well plate. In each well, 10 µL of vesicles (with Mb alone, or with GOX co-encapsulated) were mixed with 2 µL Ampliflu Red (also known as Amplex Red, AR) 100 µM, 5 µL H_2O_2 0.01%, to a final volume of 200 µL of PBS or PBS + 20 mg mL^{-1} glucose (with GOX present), and the fluorescence at 570/595 nm (±10 nm) was recorded, between 10 and 60 minutes.

Enzyme activity of β-galactosidase (β-gal)

To obtain β-gal-loaded vesicles, 100 µL of a 10 mg mL^{-1} enzyme solution was added to the reaction mixture. The enzymatic activity of β-gal was measured in a Clariostar Plus plate reader, in a Greiner transparent 96-well plate. In each well, 10 µL of vesicles encapsulating β-gal were mixed with 10 µL fluorescein Di-β-D-galactopyranoside (FDG), the formation of fluorescein was followed at 495/535 (±10) nm.

Enzyme activity of alkaline phosphatase (ALP)

To obtain ALP-loaded vesicles, 10 µL of alkaline phosphatase (13 mg ml^{-1}) were added to the reaction mixture. Once purified, the enzymatic activity of β-gal was measured in a Clariostar Plus plate reader. 10 µL of vesicles were mixed with 2 µL *para*-nitrophenylphosphate (pNPP) 1 mM, to a final volume of 200 µL in Tris-HCl. The formation of para-nitrophenol was followed at absorbance 405 nm.

The first fraction was subjected to several centrifugation and washing steps. All resulting supernatants and GUVs were incubated with trypsin (final concentration 0.5 mg mL^{-1} into 100 µL of sample) for 2 hours at 37 °C, and the resulting activities were compared to non-trypsinized samples. Volumes of both GUVs and supernatant were kept constant. The values were analysed with a t-test.

Actin polymerization

Actin was labelled with Atto 488-NHS ester, by reacting 1 mg of protein in 1 mL PBS, with 1 mM dye, 37 °C, 1 h, and then purifying the mixture with a 10 kDa spin diafiltration device (Amicon, Merck). 100 µL of actin 1 mg mL^{-1} and 10 µL of Actin-Atto 488 were added to the Mb mixture. The solvent used was Tris-HCl, pH 7.5, with the addition of 100 mM NaBr. After purification, the vesicles were imaged by diluting them either in Tris-HCl, or MgCl$_2$ 100 mM.

Calcium phosphate biomineralization

10 µL of alkaline phosphatase (ALP, 13 mg ml^{-1}) were added to the reaction mixture. In an Eppendorf tube, 100 µL of the purified sample were mixed with 50 µL calcium glycerophosphate 100 mM and 5 µL fluorescein 10 mM, then incubated at 37 °C, 4 h. The cleaving of glycerophosphate (CaGP) by ALP was confirmed visually by the formation of a white precipitate. The samples were then imaged via CLSM.

Polymerization in presence of bacteria

100 µL of *E. coli* BL21 (DE3) expressing mClover at OD$_{600}$ 1 were added to the reaction mixture. After the polymerization, the monomer conversion yield was measured via NMR spectroscopy. To image the structures, the polymer membranes were stained with Cy5-PEG$_{3.5k}$-cholesterol. For viability measurements post polymerization, non-fluorescent *E. coli* were incubated with a final 0.5 mM of fluorescein diacetate; 1 µM propidium Iodide (PI) was selected as a stain for dead cells, and substituted Cy5-PEG$_{3.5k}$-cholesterol. 100 cells per

conditions were imaged (either green or red fluorescent). Bacteria incubated at 95 °C for 10 minutes were the negative control.

Plasmid encapsulation and cell-free expression

The cell-free expression of proteins within GUVs was achieved using the Promega *E. coli* S30 Extract System for Circular DNA (L1020). 75 µl of plasmid, at different concentrations (pNCS-mClover3: 300 ng mL^{-1}; ZP9A Actin: 98.4 ng ml^{-1}; Chx10 3kb AP: 137 ng ml^{-1}), 50 µL of S30 EXTRACT (cell lysate) were added to the reaction mixture. For ZP9A Actin, 10 µL of Phalloidin Atto565 (20 µM in MeOH) were added as well. After polymerization, to 70 µL of sample, 50 µl of S30 premix (containing the energy regenerating system) and 10 µL of complete amino acid mixture were added. The sample was incubated at 37 °C for 3 h, either split in 3 wells per condition (mClover synthesis) or in Eppendorf tubes. Afterwards, they were imaged via CLSM. Actin-containing vesicles were resuspended in 100 mM MgCl$_2$, whereas ALP-containing ones were first incubated in CaGP according to the protocol described above.

Flow cytometry

For cytometric analysis of vesicles, the CytoFLEX S by Beckman Coulter was used (CytExpert Version 2.4.0.28). Samples were diluted prior to measurement with PBS to achieve an abort rate below 10%. To account for small particle size compared to cells, the primary threshold (trigger level) and the width channel were set to SSC (height: 1000). 50000 events per sample were recorded and a gating strategy was applied to exclude debris (SSC-A [log] vs FSC-A [log]) and to analyse only single vesicles per event (SSC-A [log] vs SSC-Width [linear]). Fluorescence of mClover was measured in the FITC channel (525/40 nm) at maximum gain due to small particle size.

Transmission electronic microscopy

Dry-state-stained transmission electron microscopy (TEM) imaging was performed on Tecnai Spirit transmission electron microscope (TEM, FEI/ThermoFisher, Hillsboro, Oregon, United States) operating at 120 kV using a 2k Veleta camera (Olympus, Shinjuku, Tokyo, Japan). All dry-state samples were diluted with deionized water to appropriate analysis concentration and then deposited onto GO-coated copper grids. After roughly 1 min, excess sample was blotted from the grid and the grid was stained with methylamine vanadate (Nanovan) negative stain solution for 1 min prior to blotting, drying and microscopic analysis.

Cryo-transmission electronic microscopy

A 4 µl aliquot of sample was adsorbed onto holey carbon-coated grid (Lacey, Tedpella, USA), blotted with Whatman 1 filter paper and vitrified into liquid ethane at -180 °C using a Leica GP2 plunger (Leica microsystems, Austria). Frozen grids were transferred onto a Talos Electron microscope (FEI, USA) using a Gatan 626 cryo-holder (GATAN, USA). Electron micrographs were recorded at an accelerating voltage of 200 kV using a low-dose system (40 e- Å^{-2}) and keeping the sample at -175 °C. Defocus values were -2 to 3 µm. Micrographs were recorded on 4K x 4K Ceta CMOS camera.
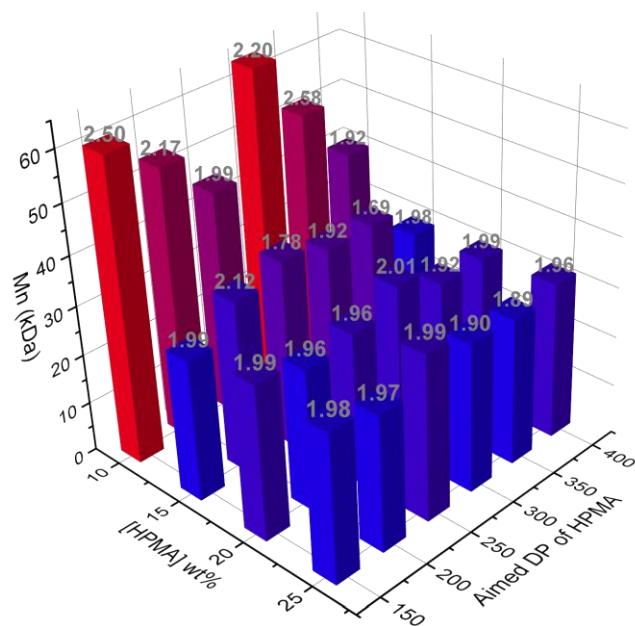
Figure S1. Molecular weight and *Đ* determined by SEC (THF, 30 °C, PS standard) of the resulting copolymer depending on the initial [HPMA] and aimed DP for bioPISA in PBS-Br. Note: as the molecular weight were around 30 kDa for [HPMA] > 10wt%, this suggests that the aimed DP is not the real DP and the important parameter could be the initiator concentration as was demonstrated for RAFT by Khor *et al*.[105]
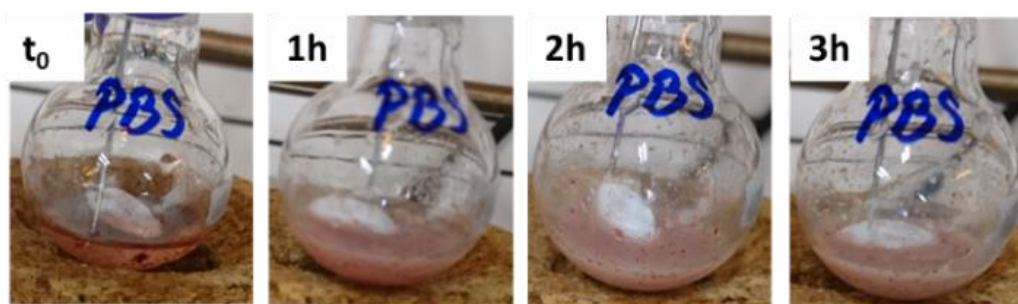

Figure S2. Photos of a bioPISA reaction mixture (DP 150 10 wt%) taken over time. The progressive increase in turbidity is due to the formation of nanostructures.

Reaction conditions

In control reactions, no reaction occurred without monomer, whereas reactions in which either mPEG-BiB, NaAsc, or Mb were omitted proceeded with a low monomer consumption of <20%. Thus, a low level of blank reaction happened, but the initiator, oxidising agent, and the metallo-protein are necessary for the reaction to proceed to high conversions (**Table S1**). The organic co-solvent DMF was necessary as well, likely as stabilizer for the growing chains.[93,94] Furthermore, polymerisations were unsuccessful when they were carried out in pure PBS or in a 100 mM NaBr solution in deionised water, indicating that both the salts in the PBS buffer and the NaBr were required for the polymerisation to happen, most likely because the buffer maintained the pH and NaBr maintained an excess of halides that is need for efficient ATRP in aqueous conditions.[95]

Table S1. Details of the bioPISA reactions conditions

| EXPERIMENTS		CONDITIONS					
[HPMA] (wt%)	Aimed HPMA (DP)	mPEG-Bib (mg)	Mb (mg)	HPMA (µL)	NaAsc (mg)	DMSO (mL)	PBS (mL)
10	150	46 (1 eq)	4.7 (0.03 eq)	187 (150 eq)	11.9 (6 eq)	0.10	1.70
10	200	35 (1 eq)	3.6 (0.03 eq)	187 (200 eq)	8.3 (6 eq)	0.10	1.70
10	250	30 (1 eq)	3.1 (0.03 eq)	187 (250 eq)	7.4 (6 eq)	0.10	1.70
10	300	25 (1 eq)	2.6 (0.03 eq)	187 (300 eq)	5.9 (6 eq)	0.10	1.70
10	350	20 (1 eq)	2.0 (0.03 eq)	187 (350 eq)	4.8 (6 eq)	0.10	1.70
10	400	17 (1 eq)	1.7 (0.03 eq)	187 (400 eq)	4.0 (6 eq)	0.10	1.70
15	150	73 (1 eq)	7.4 (0.03 eq)	296 (150 eq)	17.6 (6 eq)	0.10	1.70
15	200	55 (1 eq)	5.6 (0.03 eq)	296 (200 eq)	13.1 (6 eq)	0.10	1.70
15	250	44 (1 eq)	4.5 (0.03 eq)	296 (250 eq)	10.5 (6 eq)	0.10	1.70
15	300	29 (1 eq)	3.8 (0.03 eq)	296 (300 eq)	12.0 (6 eq)	0.10	1.70
15	350	31 (1 eq)	3.2 (0.03 eq)	296 (350 eq)	7.4 (6 eq)	0.10	1.70
15	400	27 (1 eq)	2.8 (0.03 eq)	296 (400 eq)	6.4 (6 eq)	0.10	1.70
20	150	102 (1 eq)	10.4 (0.03 eq)	414 (150 eq)	24.3 (6 eq)	0.10	1.70
20	200	77 (1 eq)	7.9 (0.03 eq)	414 (200 eq)	18.3 (6 eq)	0.10	1.70
20	250	61 (1 eq)	6.2 (0.03 eq)	414 (250 eq)	14.5 (6 eq)	0.10	1.70
20	300	51 (1 eq)	5.1 (0.03 eq)	414 (300 eq)	12.1 (6 eq)	0.10	1.70
20	350	44 (1 eq)	4.5 (0.03 eq)	414 (350 eq)	10.5 (6 eq)	0.10	1.70
20	400	39 (1 eq)	4.0 (0.03 eq)	414 (400 eq)	9.3 (6 eq)	0.10	1.70
25	150	136 (1 eq)	13.9 (0.03 eq)	552 (150 eq)	32.3 (6 eq)	0.10	1.70
25	200	102 (1 eq)	10.4 (0.03 eq)	552 (200 eq)	24.3 (6 eq)	0.10	1.70
25	250	82 (1 eq)	8.4 (0.03 eq)	552 (250 eq)	19.5 (6 eq)	0.10	1.70
25	300	68 (1 eq)	6.5 (0.03 eq)	552 (300 eq)	16.2 (6 eq)	0.10	1.70
25	350	58 (1 eq)	5.9 (0.03 eq)	552 (350 eq)	13.8 (6 eq)	0.10	1.70
25	400	51 (1 eq)	5.2 (0.03 eq)	552 (400 eq)	12.1 (6 eq)	0.10	1.70
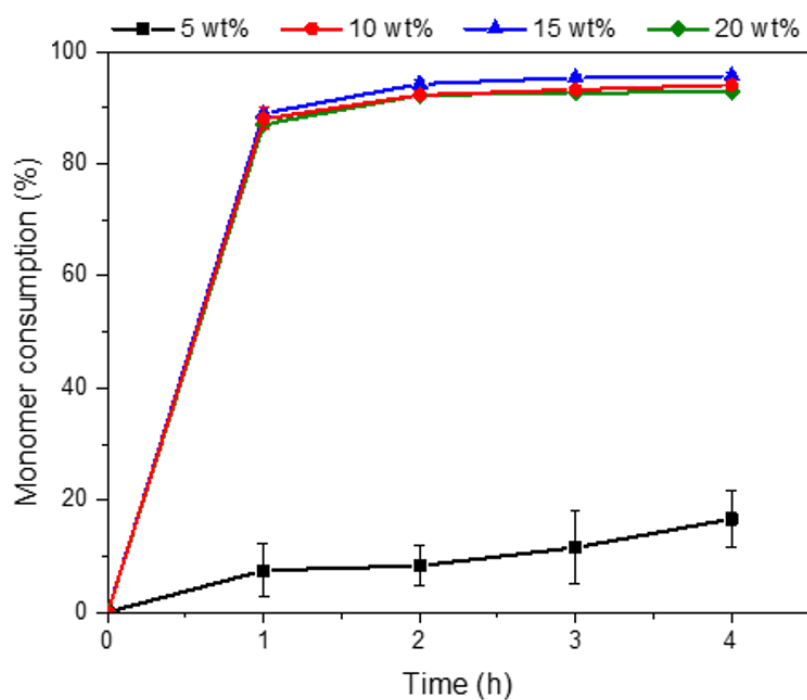
Figure S3. Monomer consumption over time ([HPMA] = 20 wt% and aimed DP = 150) at different initial monomer concentrations: 5 (black squares), 10 (red circles), 15 (blue triangles) and 20 (green diamonds) wt% with a HPMA aimed DP of 150. Error bars as mean ± SD, n = 3.
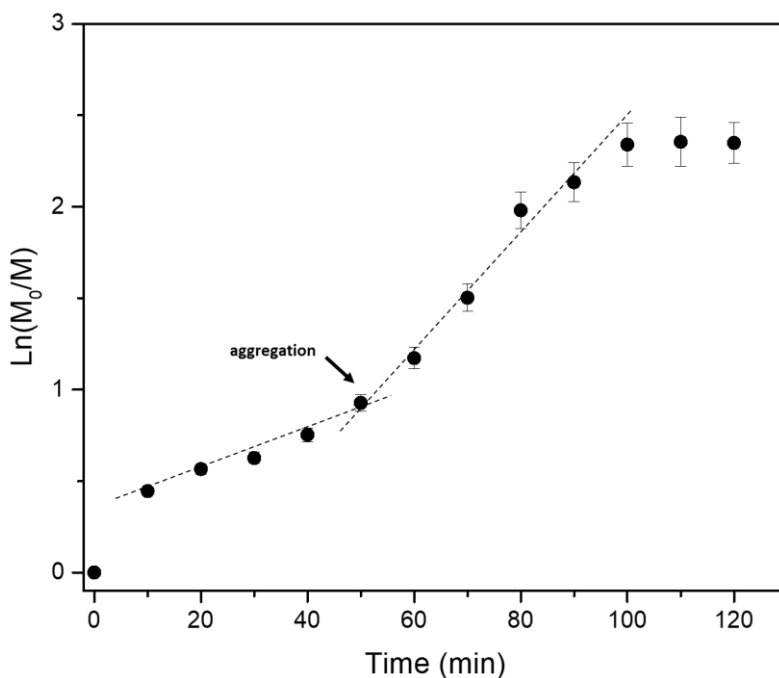

Figure S4. Kinetic data of bioPISA (DP 300 20 wt%) with 10 min intervals showing the onset of aggregation after 50 min of reaction before reaching a plateau at 100 min . Error bars as mean ± SD, n = 3.
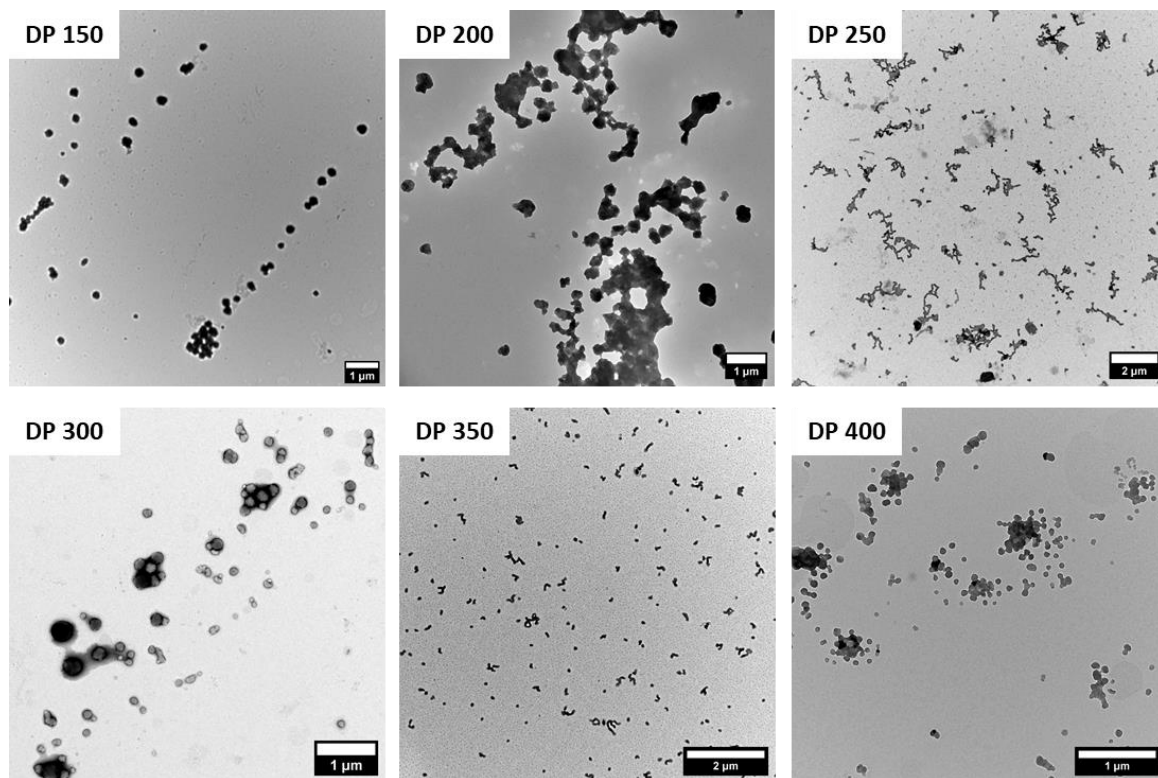
Figure S5. TEM images of morphologies from bioPISA at [HPMA] = 10 wt% and aimed DP = 150, 200, 250, 300, 350 and 400.
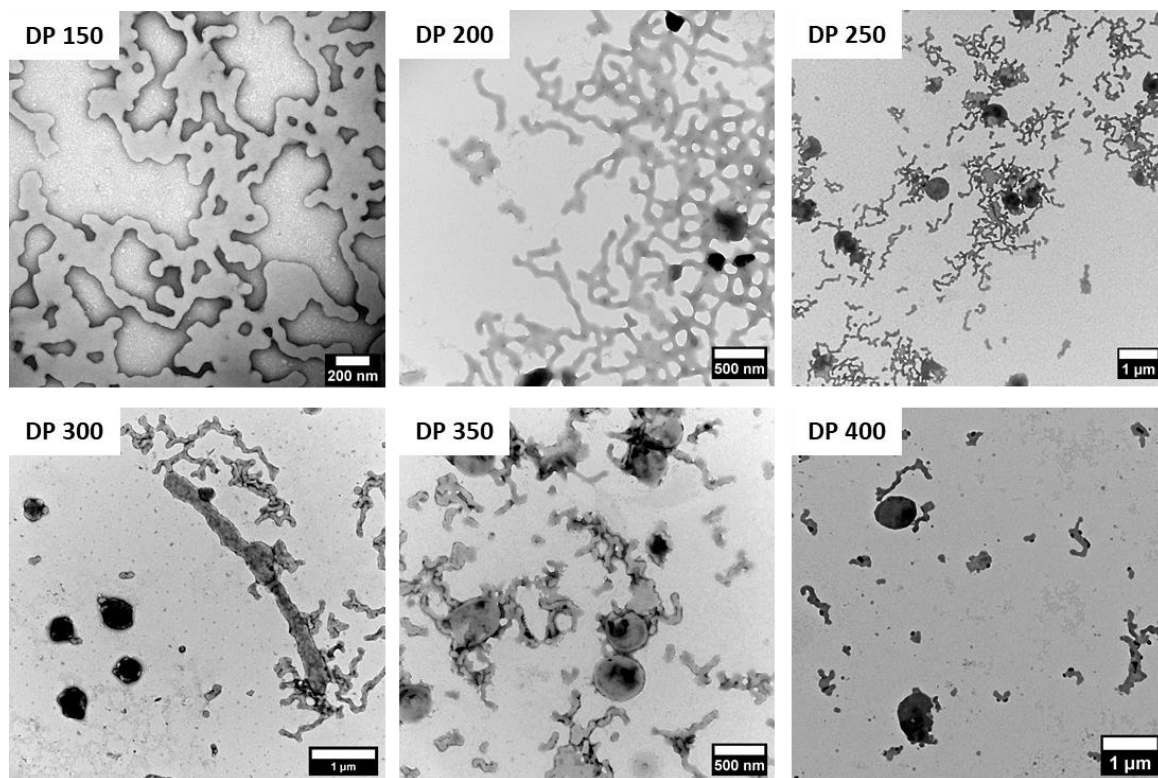
Figure S6. TEM images of morphologies from bioPISA at [HPMA] = 15 wt% and aimed DP = 150, 200, 250, 300, 350 and 400.
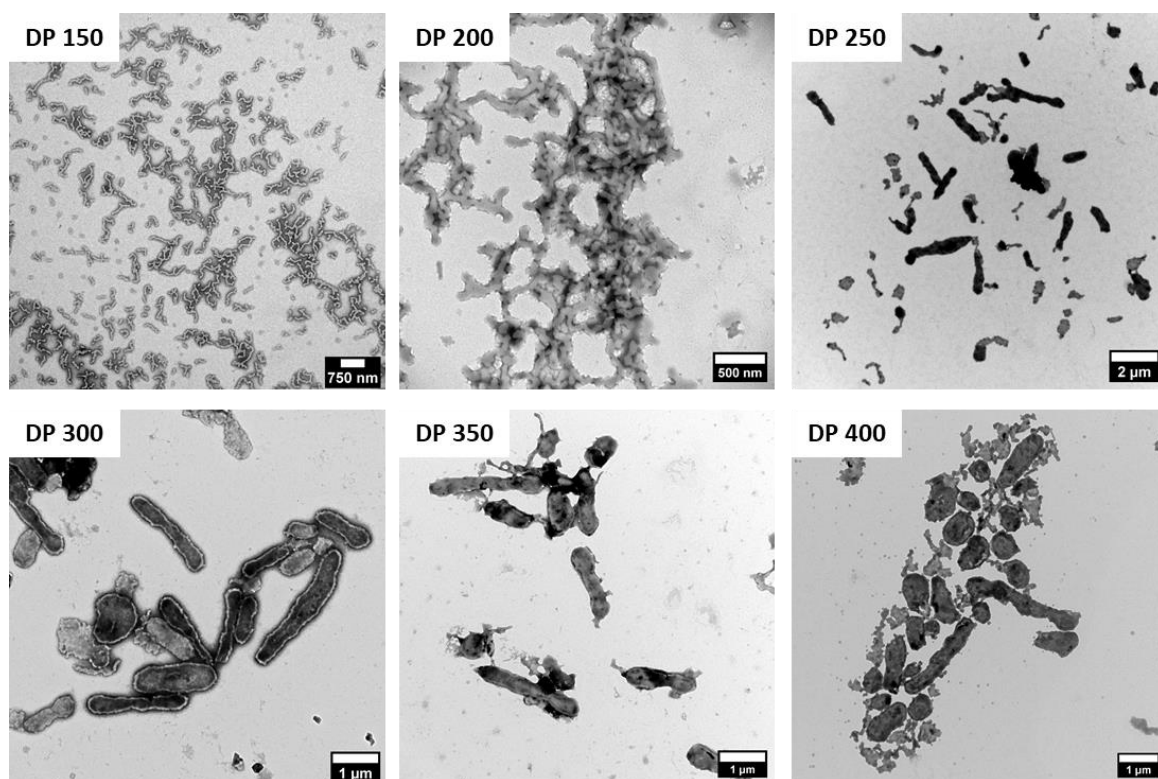
Figure S7. TEM images of morphologies from bioPISA at [HPMA] = 20 wt% and aimed DP = 150, 200, 250, 300, 350 and 400.
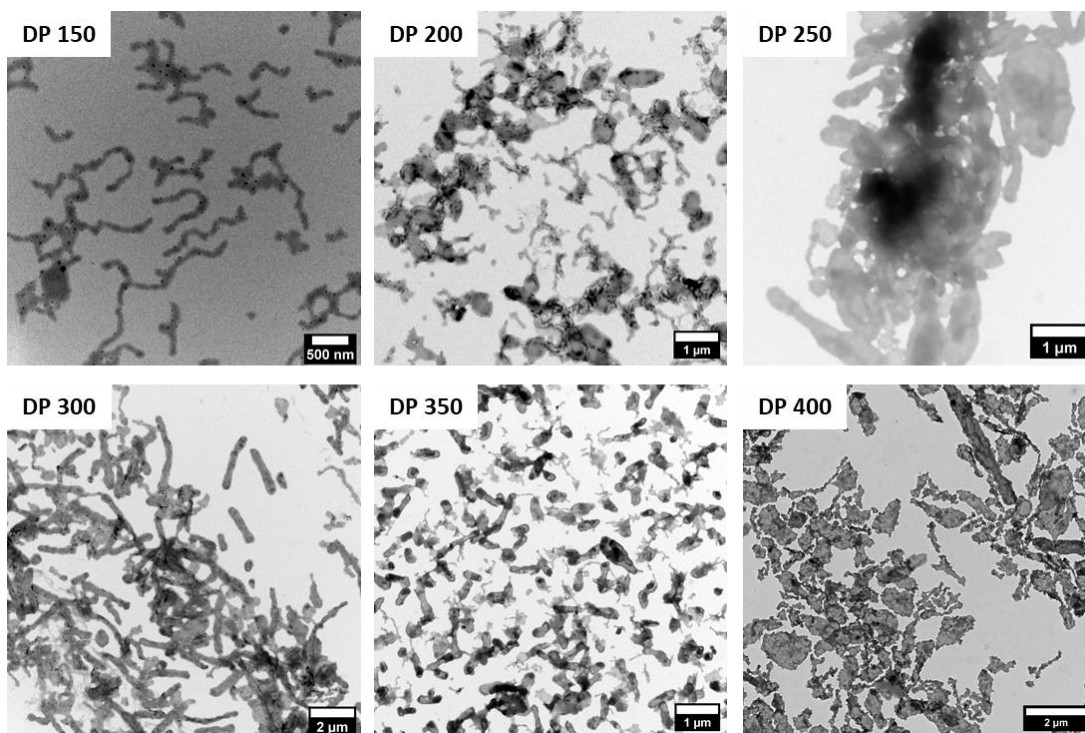
Figure S8. TEM images of morphologies from bioPISA at [HPMA] = 25 wt% and aimed DP = 150, 200, 250, 300, 350 and 400.
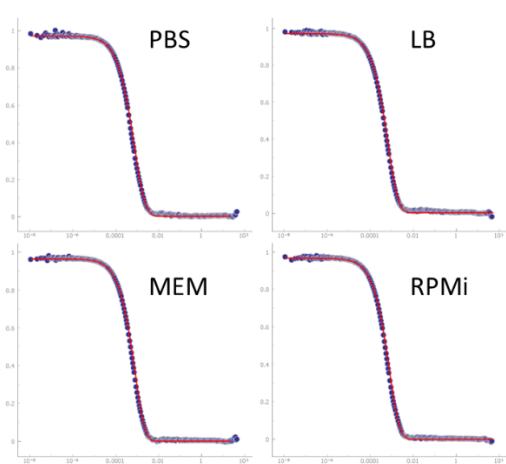
Solvent	D_h (nm)	PDI
PBS	238 ±22	0.28
LB	242 ±30	0.15
MEM	234 ±23	0.12
RPMi	208 ±24	0.12

a DLS 90 ° @ 25 °C, 10 × 60 s measurements. Cumulan

Figure S9. DLS analysis (correlograms and numerical values) of the spherical nanostructures synthesised by bioPISA in PBS-Br at [HPMA] 10 wt% and aimed DP 150.
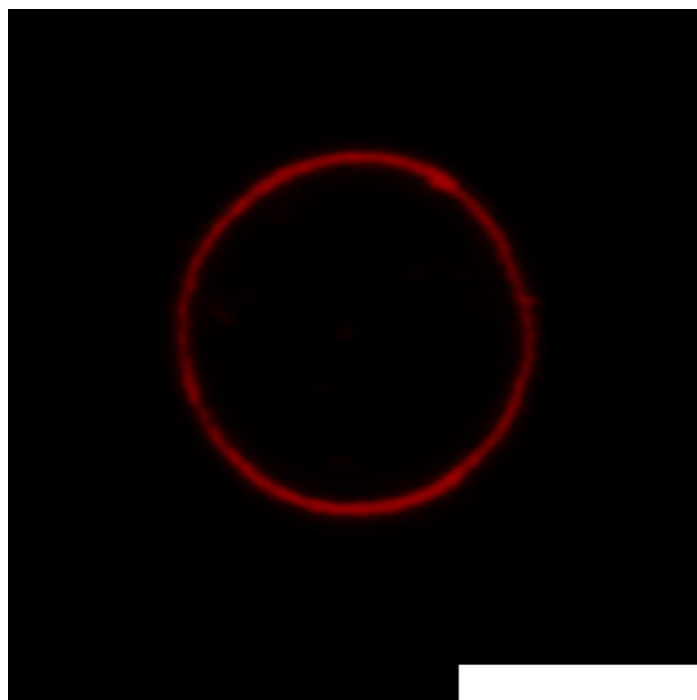
Figure S10. CLSM micrograph of a GUV obtained from bioPISA (red: Cy5-PEG$_{3.5k}$-cholesterol). Scalebar: 5 µm.
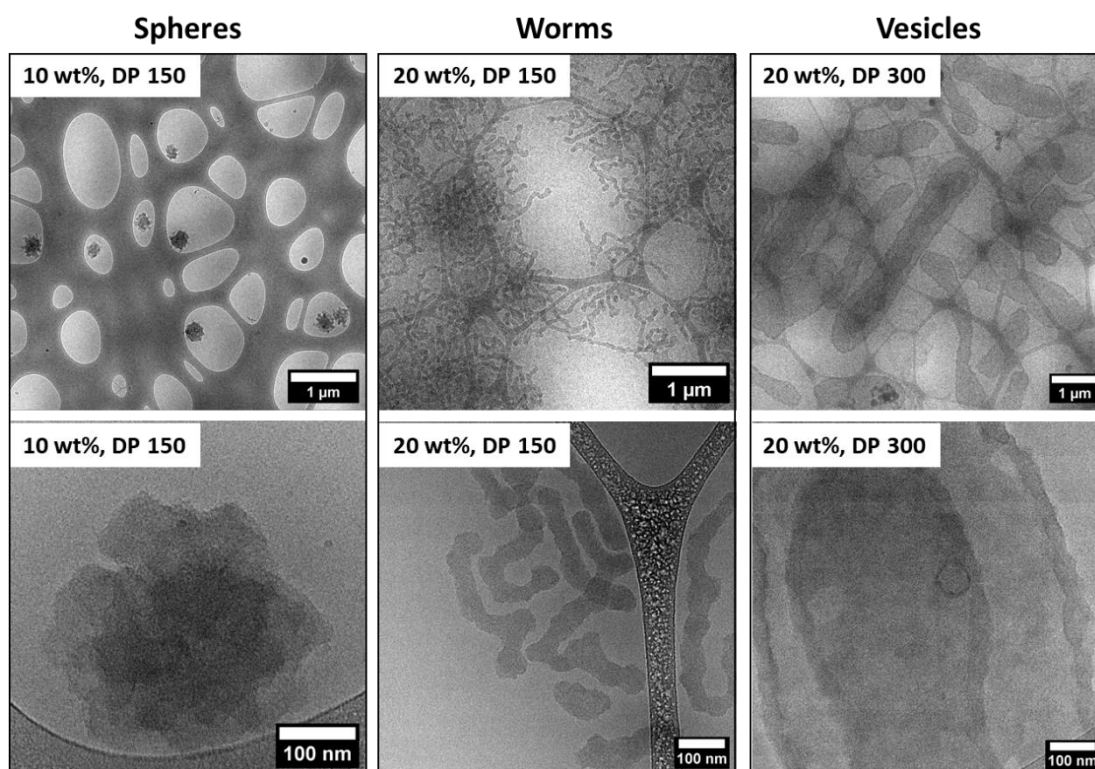
Figure S11. Cryo-TEM images of the three morphologies obtained by bioPISA in PBS-Br at [HPMA] = 10 wt% and aimed DP = 150 for the spheres, [HPMA] = 20 wt% and aimed DP = 150 for the worms and [HPMA] = 20 wt% and aimed DP = 300 for the vesicles.

Size exclusion chromatography

The polymer was only partially soluble in the organic solvent. Several other solvents (DMF, DMSO, CH_2Cl_2, $CHCl_3$) were employed, but none achieved complete dissolution of the copolymer precipitate. It is hypothesised that cross-linking happened during the chain-extension, possibly due to transesterification of the side chains once inaccessible to the catalyst, which rendered part of the final copolymer insoluble.[96,97] The fraction of insoluble copolymer was 62% ± 8% irrespective of the molecular weight of the formed polymers or the morphology of the self-assemblies. The soluble parts of the bioPISA-derived diblock copolymers had number average molecular weights (M_n) of 30-60 kDa and dispersities ($Đ$) of 1.5-2.5 (**Figure S12** and **Table S1**). One explanation for the broad molecular weight distributions is that, unlike bioRAFT where the polymer chain does not need proximity to the enzyme to grow, ATRP necessitates the catalyst for the atom transfer (in this case Mb) to be close to the active polymer chain-end.[98] In PISA, the growing chain-ends are located in the hydrophobic core or membrane of the self-assemblies, and therefore difficult for the water-soluble enzyme to reach. This most likely led to a reduction in the degree of control of the polymerization and, as a result, in high dispersities. Thus, most likely the reaction proceeded through an ATRP-like initiation and initial RDRP until the block copolymers become water-insoluble, followed by a free radical polymerisation inside of the hydrophobic parts of the formed self-assemblies. While this might seem to be a disadvantage, it did not significantly affect the predictability of our method in generating a variety of self-assembled nanostructures, as discussed above.
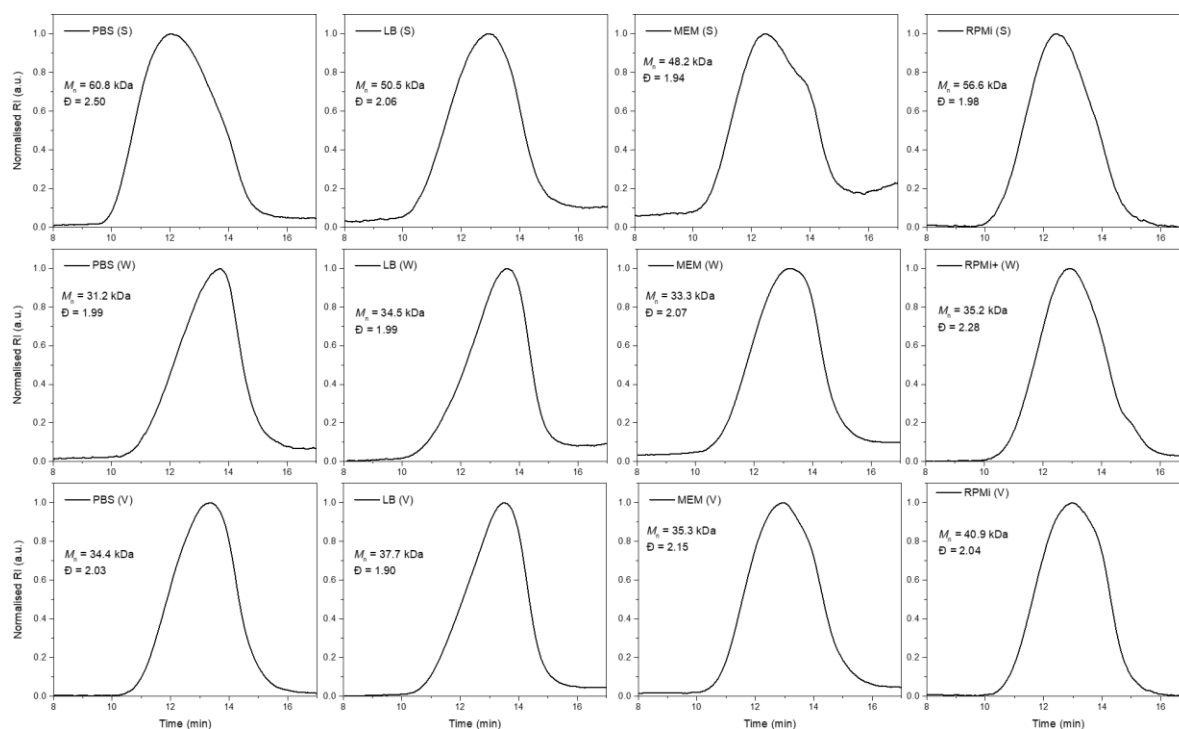
Figure S12. SEC (THF, 30 °C, PS standard) chromatogram of the purified mPEG-*b*-PHPMA copolymers from different morphologies (spheres: [HPMA] = 10 wt% and aimed DP = 150, worms: [HPMA] = 20 wt% and aimed DP = 150, vesicles: [HPMA] = 20 wt% and aimed DP = 300) synthesised by bioPISA in different media (PBS, LB, MEM and RPMi).
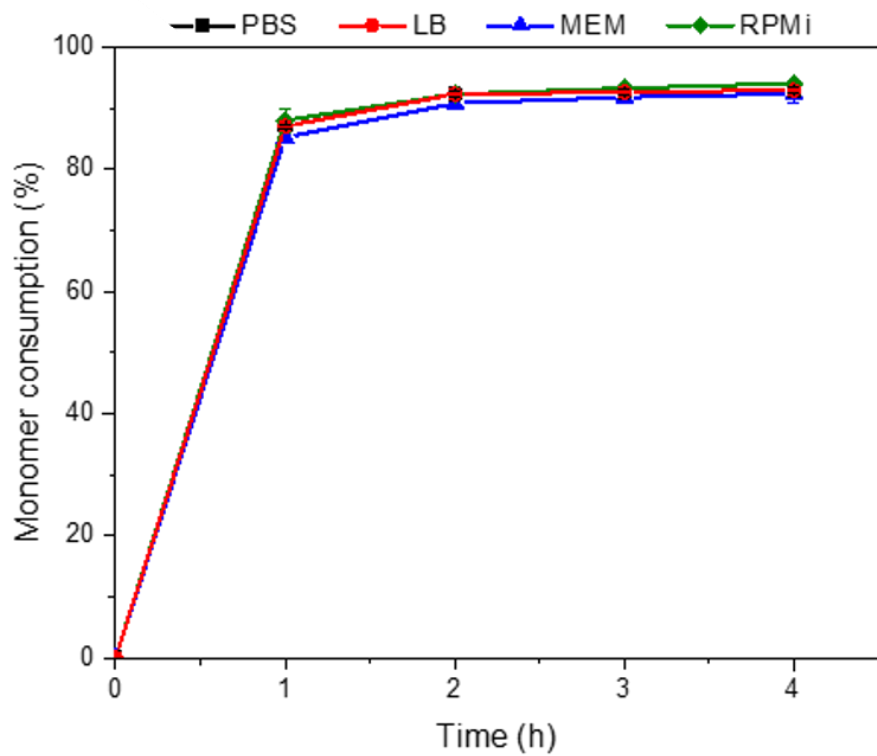
Figure S13. Monomer consumption over time ([HPMA] = 20 wt% and aimed DP = 150) in different media: PBS (black squares), LB broth (red circles), MEM (blue triangles) and RPMi-1640 (green diamonds). Error bars as mean ± SD, n = 3.
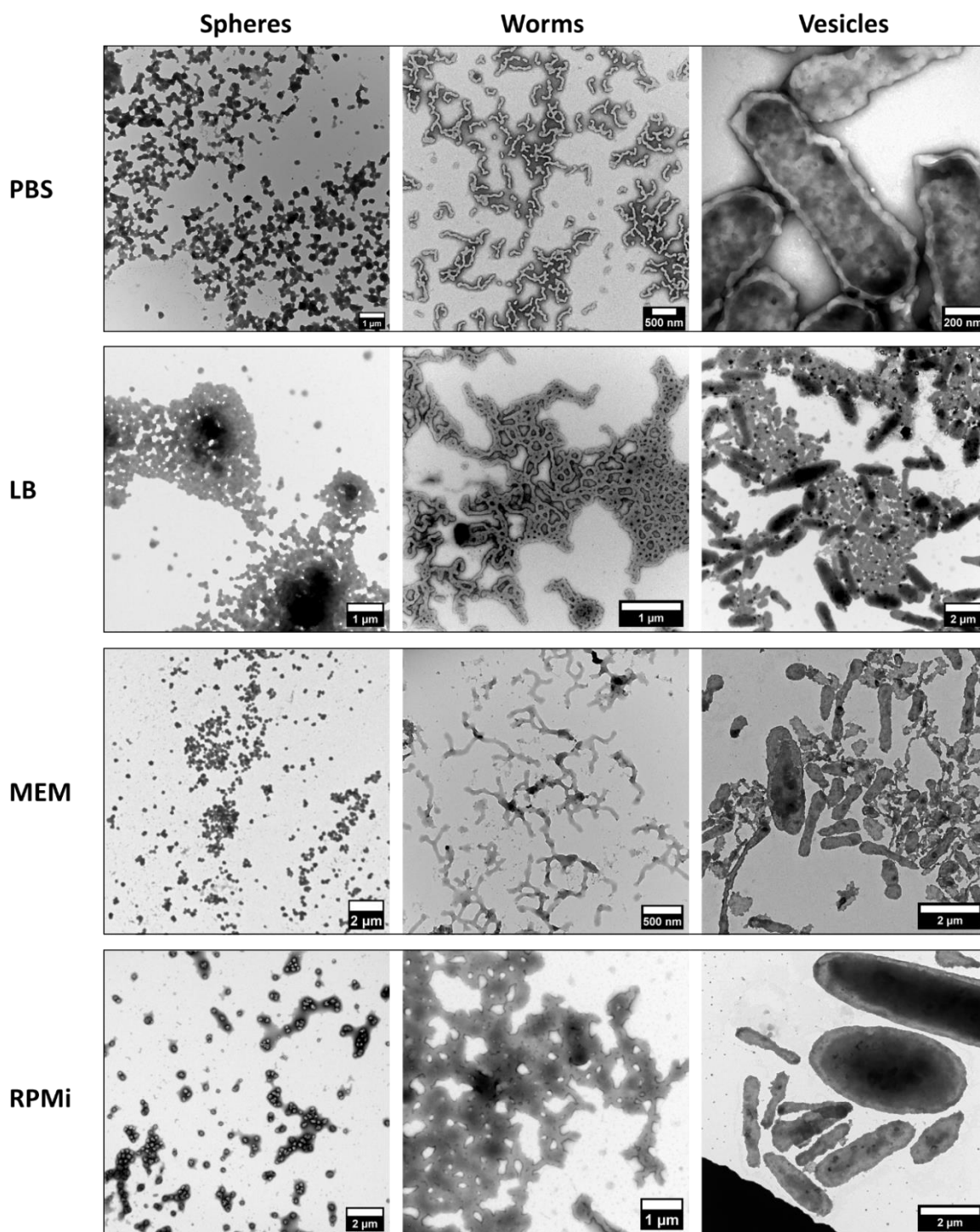
Figure S14. TEM images of the three morphologies obtained by bioPISA in different complex aqueous media (PBS, LB, MEM, RPMi) at [HPMA] = 10 wt% and aimed DP = 150 for the spheres, [HPMA] = 20 wt% and aimed DP = 150 for the worms and [HPMA] = 20 wt% and aimed DP = 300 for the vesicles.

Biocompatibility and bacterial encapsulation

To test the compatibility of bioPISA with living cells, bioPISA reactions were performed in the presence of bacteria. After bioPISA the bacteria were both inside and outside of the self-assembled polymer structures. Although either the interactions of *Escherichia coli* with the polymer chains, or the extracellular environment altered the self-assembly process, resulting in filled microparticles (**Figure S15**), we could observe spatial association of the bacteria with the polymer and encapsulation of the bacteria within the polymer structures. Importantly, the live/dead assay for bacteria showed a good viability (~70%) of these cells despite the use of an oxygen-free buffer that furthermore did not contain any nutrients and was rich in bromide ions, suggesting the biocompatibility of bioPISA (Figure S16).
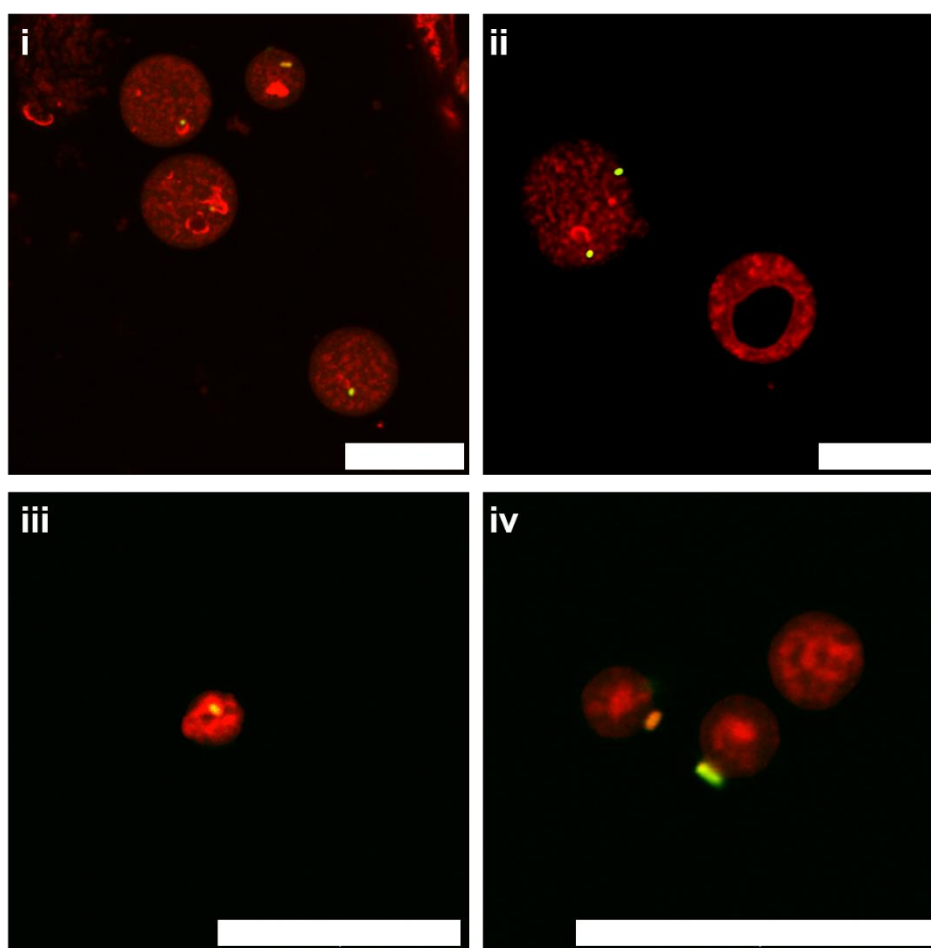
Figure S15. i-iv) Several CLSM micrographs of bioPISA-derived microparticles containing fluorescent *E. coli*. (Green: mClover expressed in *E. coli*, red: Cy5-PEG$_{3.5k}$-cholesterol). Scalebars: 20 µm.
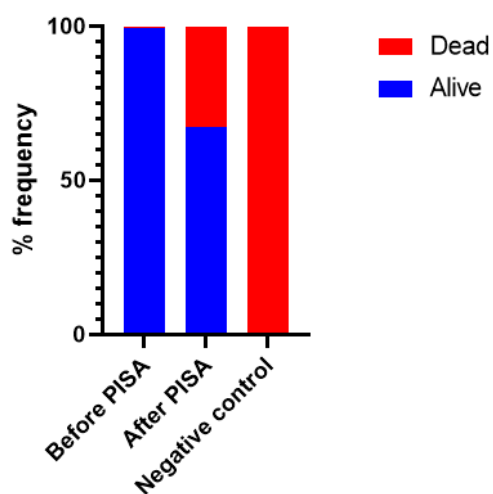
Figure S16. Live/dead assay of bacteria, showing their survival during bioPISA in PBS-Br. The negative control was provided by cells incubated at 95 °C for 10 minutes.

Reaction overview

Table S2. Overview of the bioPISA reactions and copolymers characterisation

[HPMA] (wt%)	Aimed HPMA DP	Solvent	M_n (kDa)[a]	$Đ$[a]	Monomer consumption (%)[b]	Morphology[c]
5	150	PBS	-	-	17	-
5	200	PBS	-	-	44	-
5	250	PBS	-	-	39	-
5	300	PBS	-	-	44	-
5	350	PBS	-	-	56	-
5	400	PBS	-	-	53	-
10	150	PBS	-	-	13[d]	-
10	150	PBS	-	-	15[e]	-
10	-	PBS	-	-	12[f]	-
10	150	PBS	60.8	2.50	95	Spheres
10	150	LB	50.5	2.06	94	Spheres
10	150	MEM	48.2	1.94	88	Spheres
10	150	RPMi	56.6	1.98	92	Spheres
10	200	PBS	54.2	2.17	92	Mixed
10	250	PBS	45.2	1.99	95	Mixed
10	300	PBS	64.6	2.20	78	Spheres
10	350	PBS	51.9	2.58	60	Mixed
10	400	PBS	40.0	1.92	38	Mixed
15	150	PBS	28.5	1.99	96	Worms
15	200	PBS	34.8	2.12	92	Worms
15	250	PBS	37.7	1.78	87	Mixed
15	300	PBS	35.3	1.92	94	Mixed
15	350	PBS	35.5	1.69	86	Mixed
15	400	PBS	29.1	1.98	39	Mixed
20	150	PBS	31.2	1.99	93	Worms
20	150	LB	35.0	1.98	93	Worms
20	150	MEM	33.3	2.07	93	Worms

20	150	RPMi	35.0	2.09	95	Worms
20	200	PBS	28.5	1.96	94	Worms
20	250	PBS	30.2	1.96	91	Mixed
20	300	PBS	34.4	2.01	95	Vesicles
20	300	LB	34.7	1.91	90	Vesicles
20	300	MEM	35.3	2.15	90	Vesicles
20	300	RPMi	37.6	2.05	95	Vesicles
20	350	PBS	30.0	1.92	96	Vesicles
20	400	PBS	30.0	1.99	95	Vesicles
25	150	PBS	29.9	1.98	93	Worms
25	200	PBS	27.3	1.97	94	Mixed
25	250	PBS	33.4	1.99	94	Vesicles
25	300	PBS	29.9	1.90	95	Vesicles
25	350	PBS	29.5	1.89	95	Vesicles
25	400	PBS	31.4	1.96	95	Vesicles

[a] Determined by SEC (THF, 30 °C, PS standard). [b] Determined by ^{1}H NMR spectroscopy (DMSO-d_6). [c] Determined by dry-state TEM microscopy. [d] Control reaction without NaAsc. [e] Control reaction without Mb. [f] Control reaction without mPEG-Bib.

Encapsulation and membrane permeability
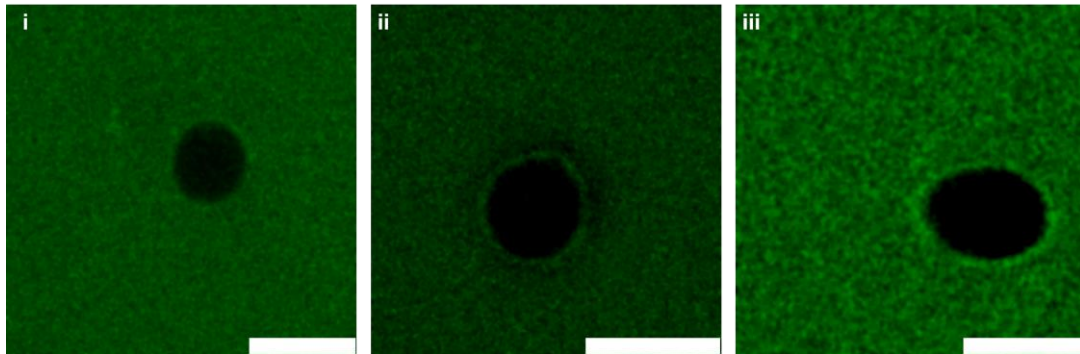
Figure S17. i-iii) Several CLSM micrographs of GUVs in a solution of FITC-Dextran 40 kDa. The vesicles are not fluorescent due to the impermeability of the membrane for the fluorescent dye (Green: FITC-Dextran 40 kDa). Scalebars: 10 µm.

Purification of GUVs via size-exclusion chromatography

Short PD 10 desalting columns have a claimed retention cut-off of 5000 Da. However, they were also previously reported to be able to separate low-concentration of proteins from vesicles.[100] To test whether they could be used for the separation of GUVs and cargo proteins, we recovered the first fraction (vesicles), washed it 1x with PBS, and then measured the Mb activity of the fractions before and after the washing steps, showing that the washed Mb-loaded GUVS had a similar activity than the original 1st fraction while the supernatant after washing had a much lower activity compared to the washed vesicles (**Figure S18**a). Thus, active protein of the 1st fraction resided in the vesicles and not in the surrounding solution. Similarly, the protein content in the vesicle-free supernatant was much lower than in the vesicles (**Figure S18**b). Finally, GUVs encapsulating ALP were washed during 4 cycles, and incubated with trypsin (0.5 mg mL^{-1}) for 1 hour. Both vesicles before and after washing retained their activity regardless of trypsinization, whereas the little activity detected in supernatants was annihilated with enzymatic digestion (**Figure S18**c), thus confirming the successful purification of free enzyme from the GUVs.
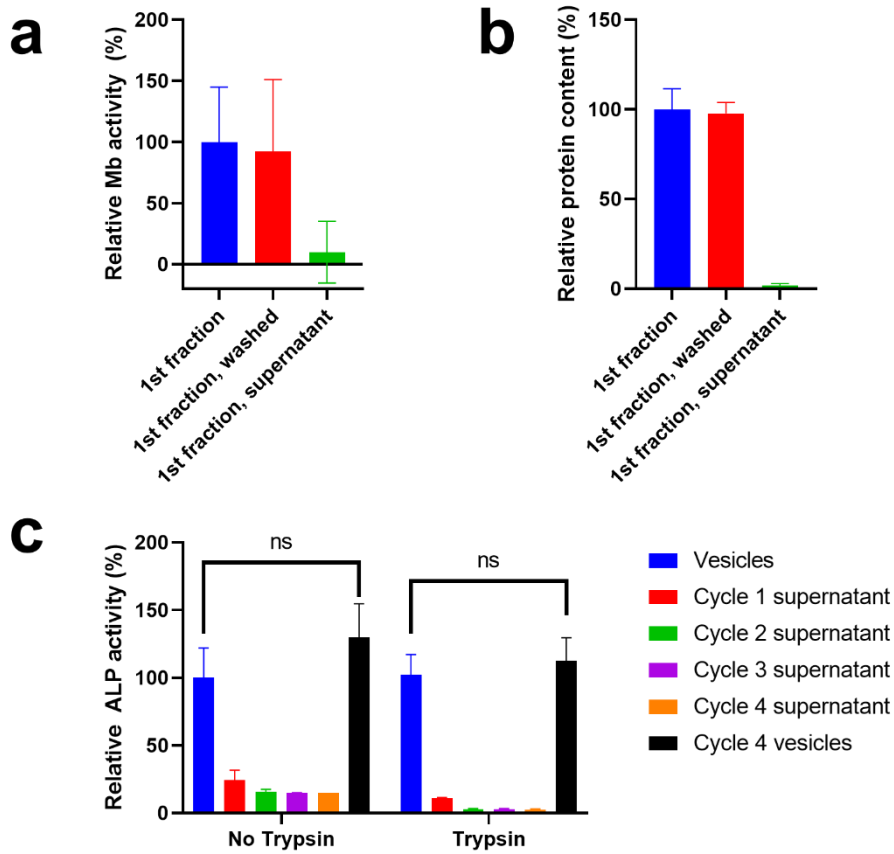
Figure S18. Purification of GUVs using PD 10 desalting columns. a) Relative Mb activity (oxidation of Ampex Red) from GUVs, GUVs after washing and resulting supernatant. b) Relative protein content from GUVs, GUVs after washing and resulting supernatant. c) Relative ALP activity (production of pNP from pNPP) of several fractions, with and without trypsin treatment. Mean ± SD, n=3.
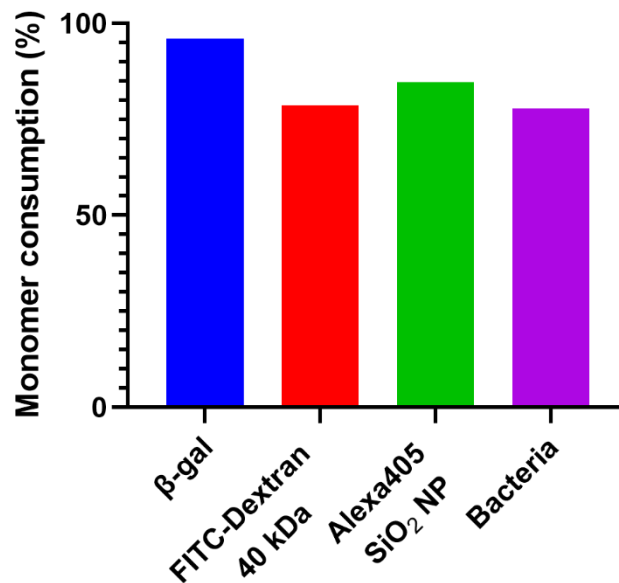
Figure S19. Monomer consumption during bioPISA in the presence of a selection of cargoes, showing the general tolerance of bioPISA for these bulky payloads.

Actin polymerization

The resulting structures were similar to intracellular phase transitions driven by intrinsically disordered proteins, rather than previously seen filaments (**Figure S20**).[101] These structures could not be observed in absence of Mg^{2+}(**Figure S21**), nor with only the added cation, without actin (**Figure S22**), confirming that only the interplay between polymerized actin and polymer membrane yielded these unique structures.
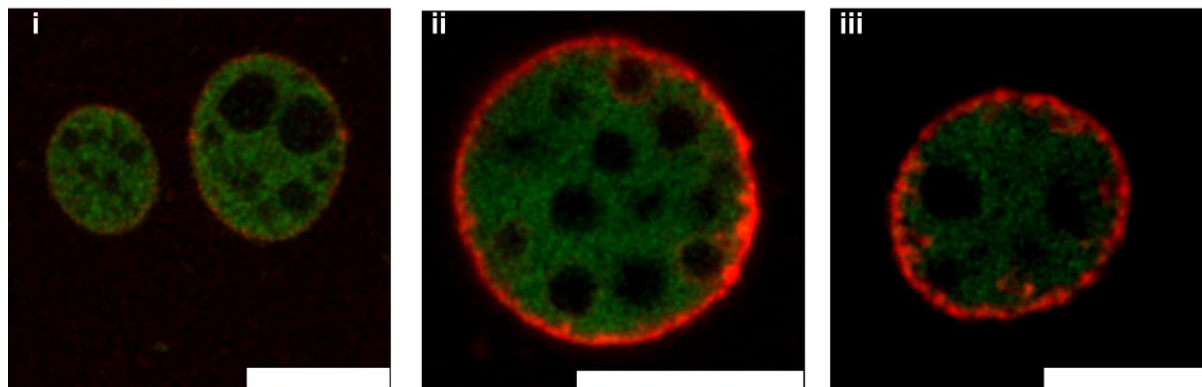
Figure S20. i-iii) Several CLSM micrographs of GUVs after the formation of actin condensates (actin/actin-Atto488/filamin: 1/0.25/0.01 weight ratio; green: actin-Atto488, red: Cy5-PEG$_{3.5k}$-cholesterol; the cholesterol dye could only label some of the inner vesicles)The cholesterol dye could only label some of the inner vesicles. Scalebars: 10 µm.
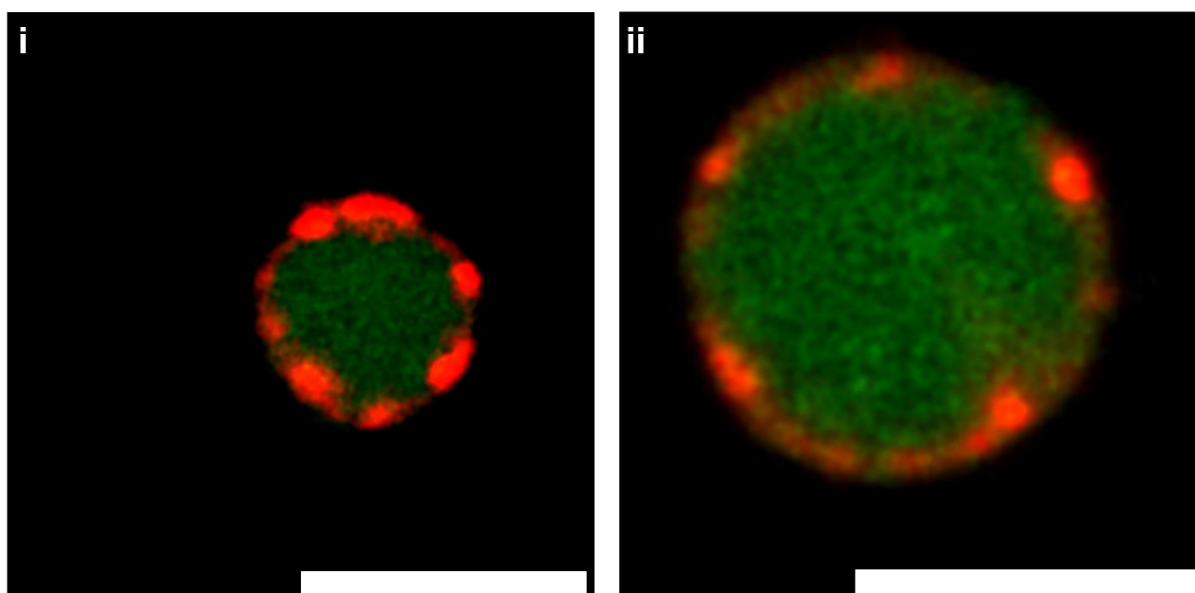
Figure S21. i-ii) Several CLSM micrographs of GUVs before the formation of actin condensates (actin/actin-Atto488/filamin: 1/0.25/0.01 weight ratio; green: actin-Atto488, red: Cy5-PEG$_{3.5k}$-cholesterol; the cholesterol dye could only label some of the inner vesicles)The cholesterol dye could only label some of the inner vesicles. Scalebars: 5 µm.
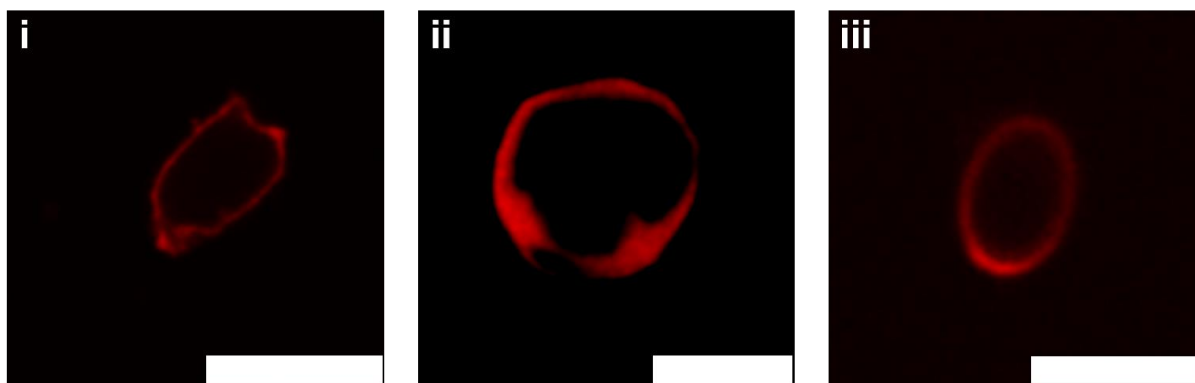
Figure S22. i-iii) Several CLSM micrographs of GUVs after addition of MgCl$_2$. Red: Cy5-PEG3.5k-cholesterol. The higher magnesium ion concentration appears to produce some deformations in the GUVs, but no subcompartment can be observed. Scalebars: 10 μm.
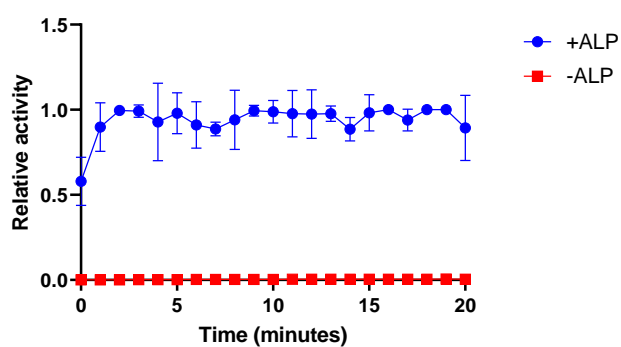

Figure S23. Activity of encapsulated ALP in bioPISA GUVs hydrolysing *p*-nitrophenyl phosphate (pNPP) to produce the phosphate-less coloured species pNP, showing that the enzyme is still active in the GUVs. All values displayed as mean ±SD, n=3 replicates for all experiments.
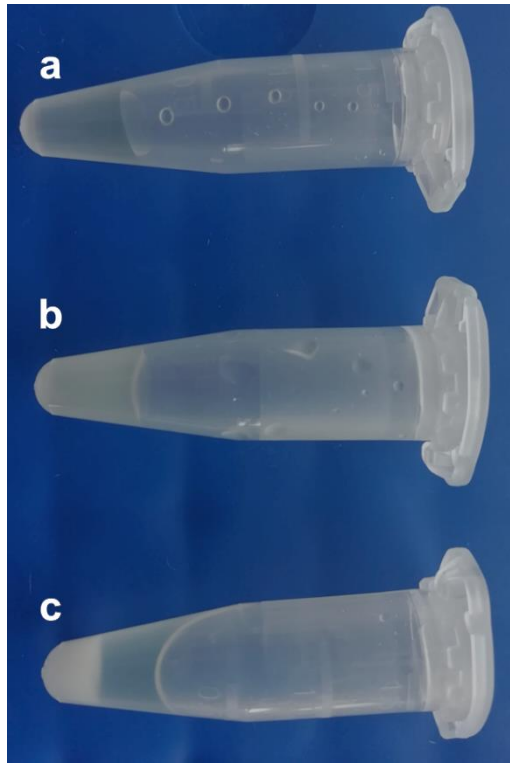
Figure S24. Co-precipitation of calcium phosphate and ALP in GUVs. a) CaGP, no GUVs. b) GUVs, no CaGP. c) GUVs + CaGP, leaving a clear supernatant in the last sample.
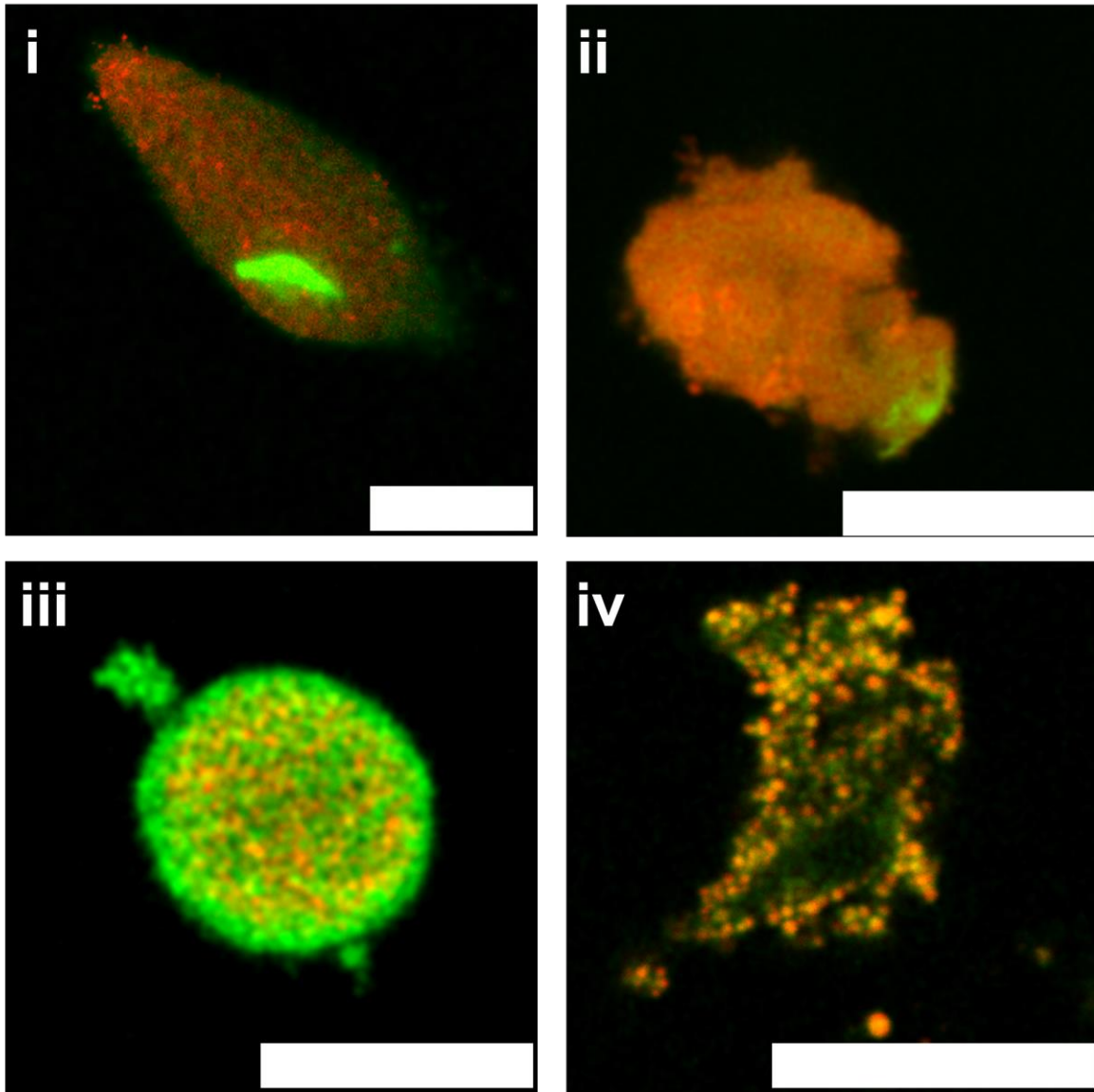
Figure S25. i – iv) Several CLSM micrographs of GUVs after the biomineralization of CaGP by ALP. Green: calcium phosphate-adsorbed fluorescein. Red: Cy5-PEG3.5k-cholesterol. Scalebars: 10 μm.
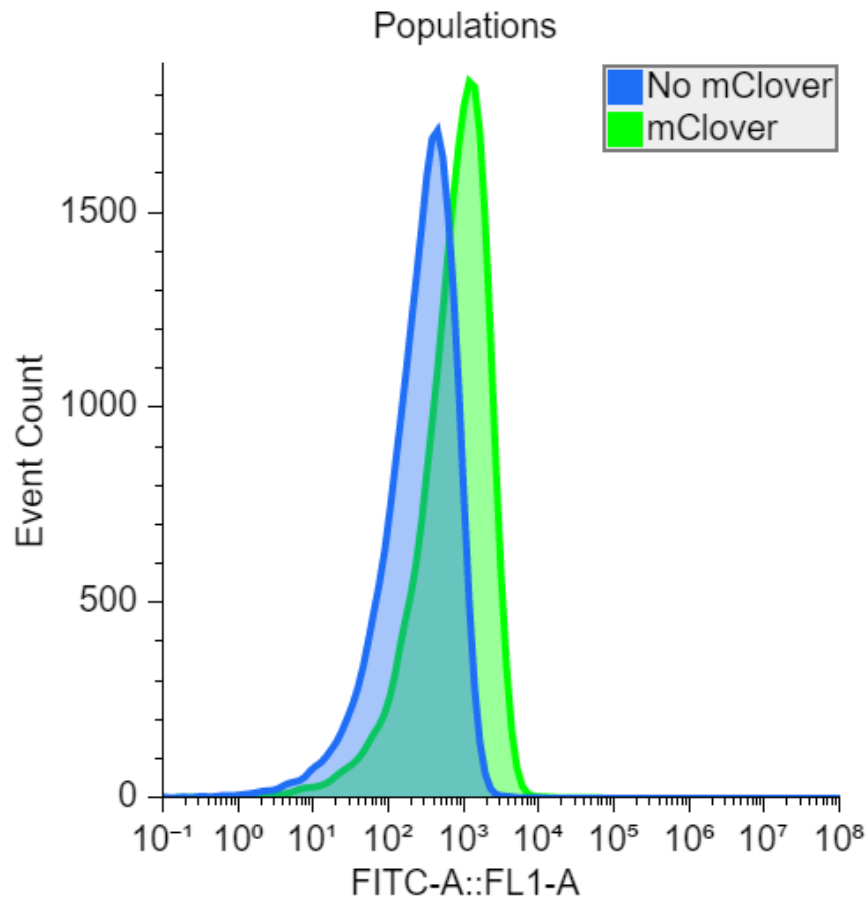
Figure S26. Flow cytometry fluorescence distributions for GUVs without and with plasmid, after the expression of mClover in the GUVs.
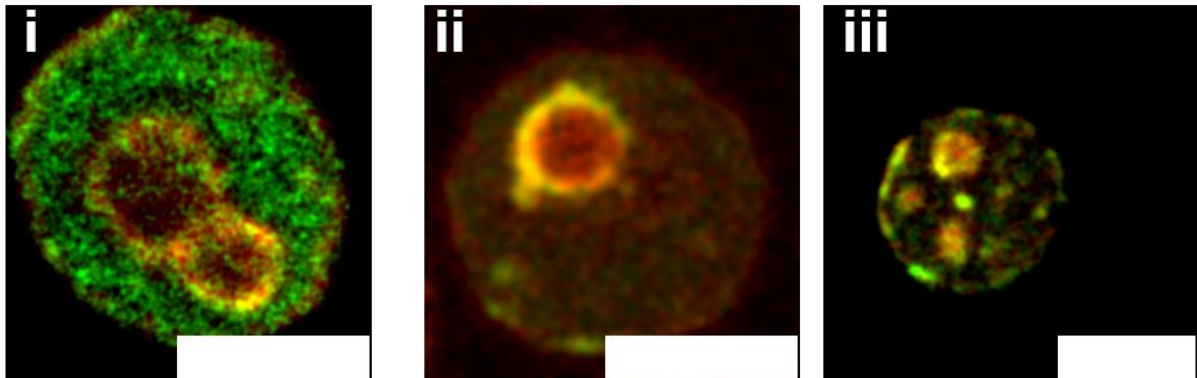
Figure S27. i – iii) CLSM micrographs of GUVs with expressed actin + phalloidin-Atto565 (green: phalloidin-Atto565, red: Cy5-PEG$_{3.5k}$-cholesterol. Scalebars: 10 µm. Actin expression levels likely vary from GUV to GUV, and thus the morphologies it produces.
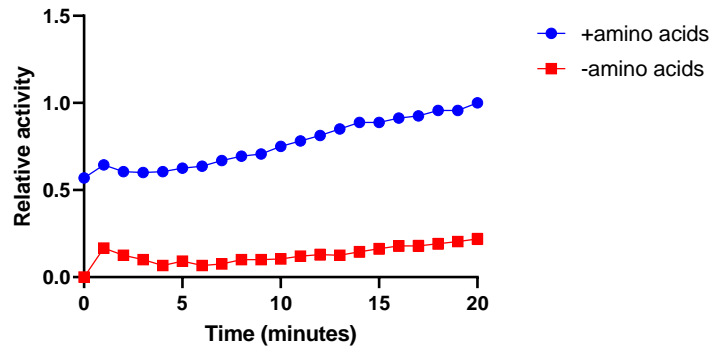
Figure S28. Activity of GUVs expressing ALP (decreased expression without supplemented amino acids) hydrolysing *p*-nitrophenyl phosphate (pNPP) to produce the phosphate-less coloured species pNP, plateauing earlier for GUVs + amino acids. All values displayed as mean ±SD (values too small to be displayed), n=3 replicates for all experiments.
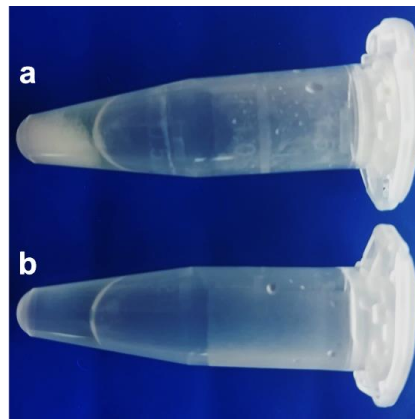

Figure S29. Co-precipitation of calcium phosphate and expressed ALP in GUVs. a) GUVs + expressed ALP + CaGP. b) GUVs + CaGP but no ALP expression.
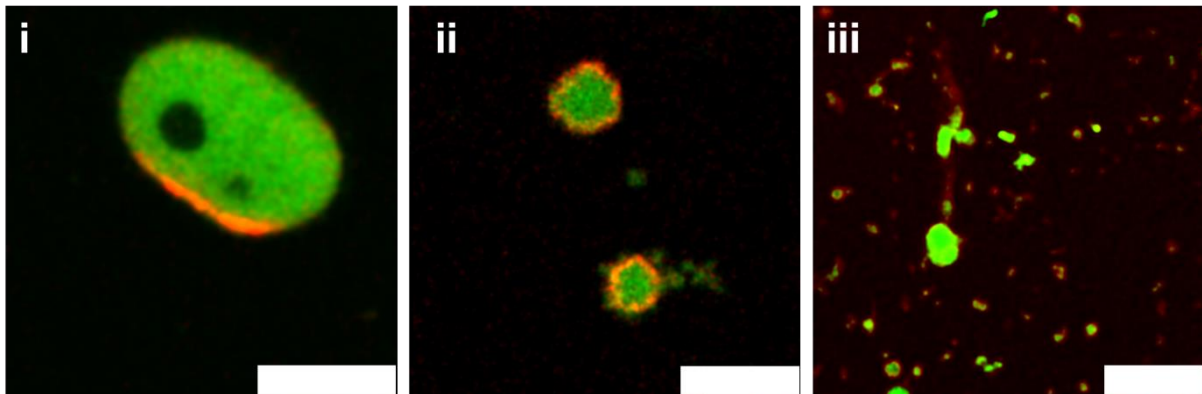

Figure S30. i-iii) Several CLSM micrographs of GUVs after the biomineralization of CaGP by expressed ALP. Green: calcium phosphate-adsorbed fluorescein. Red: Cy5-PEG3.5k-cholesterol. Scalebars: 10 μm.